ARMY RESEARCH LABORATORY

Implementation of Schoenfeld-Wright Failure Criterion Into a Three-Dimensional Adiabatic Shear Band Model in CTH

by Müge Fermen-Coker

ARL-TR-3284 **September 2004**

NOTICES

Disclaimers

The findings in this report are not to be construed as an official Department of the Army position unless so designated by other authorized documents.

Citation of manufacturer's or trade names does not constitute an official endorsement or approval of the use thereof.

Destroy this report when it is no longer needed. Do not return it to the originator.

Army Research Laboratory
Aberdeen Proving Ground, MD 21005-5066

ARL-TR-3284 **September 2004**

Implementation of Schoenfeld-Wright Failure Criterion Into a Three-Dimensional Adiabatic Shear Band Model in CTH

Müge Fermen-Coker
Weapons and Materials Research Directorate, ARL

REPORT DOCUMENTATION PAGE	Form Approved OMB No. 0704-0188

1. REPORT DATE *(DD-MM-YYYY)*	2. REPORT TYPE	3. DATES COVERED (From - To)
September 2004	Final	September 2002–September 2003

4. TITLE AND SUBTITLE
Implementation of Schoenfeld-Wright Failure Criterion Into a Three-Dimensional Adiabatic Shear Band Model in CTH

5a. CONTRACT NUMBER

5b. GRANT NUMBER

5c. PROGRAM ELEMENT NUMBER

6. AUTHOR(S)
Müge Fermen-Coker

5d. PROJECT NUMBER
AH43

5e. TASK NUMBER

5f. WORK UNIT NUMBER

7. PERFORMING ORGANIZATION NAME(S) AND ADDRESS(ES)
U.S. Army Research Laboratory
ATTN: AMSRD-ARL-WM-TC
Aberdeen Proving Ground, MD 21005-5066

8. PERFORMING ORGANIZATION REPORT NUMBER
ARL-TR-3284

9. SPONSORING/MONITORING AGENCY NAME(S) AND ADDRESS(ES)

10. SPONSOR/MONITOR'S ACRONYM(S)

11. SPONSOR/MONITOR'S REPORT NUMBER(S)

12. DISTRIBUTION/AVAILABILITY STATEMENT
Approved for public release; distribution is unlimited.

13. SUPPLEMENTARY NOTES

14. ABSTRACT
A failure criterion based on material response and scaling laws is implemented into a three-dimensional shear band nucleation and propagation model being developed in CTH, a Eulerian wave propagation code. Numerical simulations of plastic localization in Ti-6Al-4V armor plates due to steel fragment impact are carried out, before and after the implementation of the failure criterion. Adiabatic shearing is depicted as the impact speed approaches the ballistic limit velocity, confirming experimental observations. The capability to calculate Grady-Kipp and Wright-Ockendon length scales are added to CTH to be used in conjunction with the shear band model. Computational aspects of shear band spacing effects are discussed.

15. SUBJECT TERMS
shear band, adiabatic, failure, model, CTH

16. SECURITY CLASSIFICATION OF:			17. LIMITATION OF ABSTRACT	18. NUMBER OF PAGES	19a. NAME OF RESPONSIBLE PERSON
a. REPORT	b. ABSTRACT	c. THIS PAGE			Müge Fermen-Coker
UNCLASSIFIED	UNCLASSIFIED	UNCLASSIFIED	UL	44	19b. TELEPHONE NUMBER (*Include area code*) 410-278-6018

Standard Form 298 (Rev. 8/98)
Prescribed by ANSI Std. Z39.18

Contents

List of Figures

List of Tables

Acknowledgments

The author acknowledges the support of the U.S. Army Research Laboratory (ARL), Weapons and Materials Research Directorate Impact Physics Branch (IPB), and wishes to thank Dr. Scott Schoenfeld (Chief, IPB, ARL), Dr. Stewart Silling (Sandia National Laboratories, Albuquerque, NM), and Dr. Lee Magness (Lethal Mechanisms Branch, ARL) for sharing their valuable insight and expertise during many helpful discussions. Dr. Silling provided a draft copy of the CTH Reference Manual for his three-dimensional shear band model, upon which section 2 of this report is based. Dr. Tusit Weerasooriya (IPB, ARL) provided the material characterization data used in this study. Dr. Schoenfeld graciously shared details of his work (Schoenfeld and Wright, 2003).

1. Introduction

The capability to model failure associated with plastic shear localizations in ballistic applications, such as plugging failure of metal plates due to ballistic impact by blunt-nosed projectiles, has long been desirable. However, it was mostly studied experimentally, rather than computationally, due to the complexity of the failure process. Upon impact, the plate material was rapidly accelerated ahead of the projectile, creating a velocity discontinuity within the target, which gave rise to plastic localization under adiabatic conditions. Heat generated by plastic work and growth of microcracks and microvoids contributed to building damage inside the shear bands. Finally, a crack started to grow towards the back side of the target, and the material was punched out, leaving a hole in the target. During the last decade, several researchers attempted to study this problem computationally in Lagrangian framework, using erosion algorithms, element-kill techniques, etc. This report focuses on simulating shear band nucleation and propagation within the Eulerian context of CTH.

The current distribution of CTH does not have plastic localization capability and therefore cannot be effectively used to model some problems of interest in ballistics, such as self-sharpening behavior associated with penetrator materials susceptible to shear localizations, as well as failure of armor plates via plugging. As reported by Magness and Farrand (1990), certain uranium alloys exhibited considerably better penetration performance compared to tungsten heavy alloys with similar density and mechanical properties. Shear bands have been suggested and later numerically shown to be a factor in the improved ballistic performance of depleted uranium penetrators, using a two-dimensional (2-D) ad-hoc shear band model in CTH (Silling, 1993). A brief history of the earlier 2-D model and a description of the new three-dimensional (3-D) model are given in section 2.

The two examples of failure due to shear localization previously described as well as a block of homogenous material subject to shear due to an imposed internal velocity discontinuity were studied using the shear band model. However, only shear bands in armor plates due to fragment impact is covered in this report, primarily to maintain focus and also because accumulated data to reach the conclusions was sufficiently sampled using this example. The experimental results by Burkins et al. (1997) were used to validate the numerical results.

The implementation of a failure criterion recently published by Schoenfeld and Wright (2003) to replace previously user-specified plastic strain and strain rate criteria for shear band nucleation in CTH is discussed in section 3. The criterion is based on ideas developed by Wright (1992, 1994) and uses material response and scaling laws to estimate the plastic strain at which stress collapse due to adiabatic shear should occur for rate-dependent, work-hardening, thermally softening materials. A comprehensive summary of the theory is provided by Wright (2002). Details of the development of the failure criterion will not be

repeated in this report since it was provided in the aforementioned paper (Schoenfeld and Wright, 2003), where they also discussed its implementation into a Lagrangian wave propagation code EPIC, implications of the model for material failure simulations, and its employment to analyze boundary value problems dominated by shear failure. Their examples included uniaxial compression, a strong velocity discontinuity that simulates edge impact by the edge of a cutting tool or a projectile, and the fragment impact problem, which is also used as an example in this report.

A brief description of the fragment impact problem, along with details of the computational model, and results both preceding and following the implementation of the Schoenfeld-Wright failure criterion are given in section 4. Conclusions are summarized in section 5, along with discussions regarding future work.

2. Description of the 3-D Adiabatic Shear Band (ASB) Model in CTH

The first ASB model developed and implemented into CTH by Silling (1993) was a 2-D ad-hoc model. It was designed to investigate whether or not ASB's have a direct influence on the improved performance of uranium alloys, by sharpening the nose of the penetrator, as Magness and Farrand suggested (1990). Silling modified CTH to simulate growth of individual representative shear bands. The growth direction for the bands was artificially set to point toward the tip of the penetrator, per micrographic evidence. The two materials compared were similar to tungsten alloys, with and without shear band capability, to assess the difference in ballistic performance solely due to effects of shear bands. Silling concluded that the penetration depth could be improved significantly due to shear bands at low impact velocities, and the improvement decreased as the impact velocity increased. It also indicated that there was an optimal critical plastic strain for the onset of shear bands, along with an optimal angle of growth.

Nucleation was done explicitly by defining Lagrangian tracer particles at prescribed locations. Tracer particles in CTH, which can be Eulerian or Lagrangian, are imaginary particles that are generally used for postprocessing purposes. Lagrangian tracer particles were convected along with the deforming body. In this particular version of the code, they also represented locations along shear bands, since they were activated as the computation marched on, when the local plastic strain and strain rate exceeded respective critical values specified by the user.

The 3-D ASB model that constitutes the numerical framework for this study was more recently developed by Silling (2002). Tracer particles are used once again, to nucleate and propagate shear bands. However, nucleation is not initiated explicitly at prescribed locations

as before. Instead, the following set of nucleation criteria need to be satisfied at a point $\tilde{x}$ in order for a Lagrangian tracer particle to be introduced at that location:

$$\varepsilon(\tilde{x},t) \geq \varepsilon_{cr}^{nu}, \tag{1}$$

$$\dot{\varepsilon}(\tilde{x},t) \geq \dot{\varepsilon}_{cr}^{nu}, \tag{2}$$

$$D(\tilde{x},t) \geq D_{cr}, \tag{3}$$

and

$$D^{*}(\tilde{x},t) \geq D_{cr}^{*}. \tag{4}$$

The critical values on the right-hand side of equations 1–4 are specified by the user and are defined as follows: ε_{cr}^{nu} is the critical equivalent plastic strain for nucleation, $\dot{\varepsilon}_{cr}^{nu}$ is the critical plastic strain rate for nucleation, D_{cr} is the minimum distance requirement to any active or inactive shear band, and D_{cr}^{*} is the minimum distance to any active shear band at the time of nucleation.

Upon nucleation, a shear band is assigned an initial orientation along a plane of maximum shear. There are two such planes, corresponding to the smallest and largest eigenvalues of the strain rate tensor at the nucleation point. Each plane, oriented at a 45° angle to the principal axes, is an apparent candidate for shear band growth. The plane that corresponds to the greater velocity jump compared to the other is selected as the plane of shear band. An angular coordinate, θ, is defined in this plane, as well as a coordinate, r, which represents the path along the shear band at constant θ (figure 1). Also in the shear band plane, a set of unit vectors called the growth direction vectors is introduced as $g(\tilde{x},\theta)$. During the growth process, at any point $\tilde{x}$ on the edge of the shear band, these unit vectors provide the growth direction. A more detailed description of the model and additional figures are provided in Silling (2002).

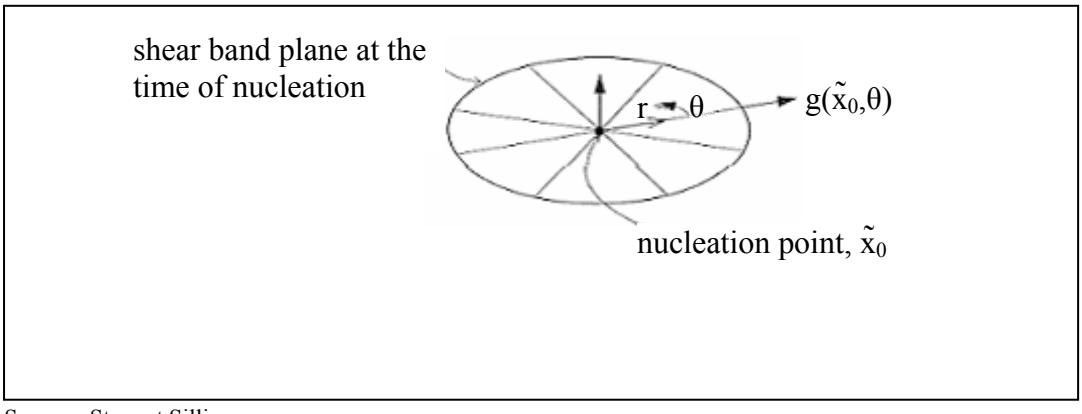

Source: Stewart Silling.

Figure 1. Shear band nucleation model.

During the preliminary numerical studies using the ASB model, yet another nucleation condition was added to have control over where the nucleation occurs, depending on the specific problem studied. In some cases, physical evidence indicated that shear bands initiate at material boundaries and free surfaces; it is of interest to validate this computationally. In other cases, it may be the opposite, and shear bands may seem to originate away from material boundaries and free surfaces. Having this flexibility in the code not only provides better comparison with experimental evidence but also the capability to investigate this phenomenon computationally. The ASB model is modified to allow the user to select one of the following nucleation options:

1. only on material boundaries and free surfaces,
2. never on material boundaries and free surfaces , and
3. anywhere the other nucleation criteria are satisfied (no preference).

Once a shear band nucleates, it is allowed to grow at any point that lies on the edge of the shear band, provided that the following criteria are satisfied:

$$\varepsilon(\tilde{x},t) \geq \varepsilon_{cr}^{gr}, \tag{5}$$

and

$$\dot{\varepsilon}(\tilde{x},t) \geq \dot{\varepsilon}_{cr}^{gr}, \tag{6}$$

where ε_{cr}^{gr} is the critical value of equivalent plastic strain for growth and $\dot{\varepsilon}_{cr}^{gr}$ is the critical value of plastic strain rate for growth.

As the shear band propagates, it conforms to the local planes of maximum shear (figure 2). If the propagation velocity is not prescribed by the user, the default growth ring spacing is set equal to the mean cell size. However, if a propagation velocity is prescribed for a material, the spacing is calculated by multiplying the prescribed velocity by the time step. The shear band then is allowed to grow at its edge at the specified propagation velocity parallel to the growth direction vector at each θ. For all the numerical results reported herein, the growth ring spacing is set equal to the mean cell size, by default.

The shear band propagation is arrested in directions along the current edge of the shear band where the growth criteria are not satisfied. However, the shear band is considered to be active and can keep propagating as long as the growth criteria are met at least one point along the current edge of the shear band. It only becomes inactive when growth is arrested for all θ, $0 \leq \theta < 2\pi$. Once a shear band becomes inactive, propagation is never permitted to start again, even if the growth criteria are met at a later time along the edge; this simulates the assumption that the interior of the shear band cools off quickly and hardens when growth

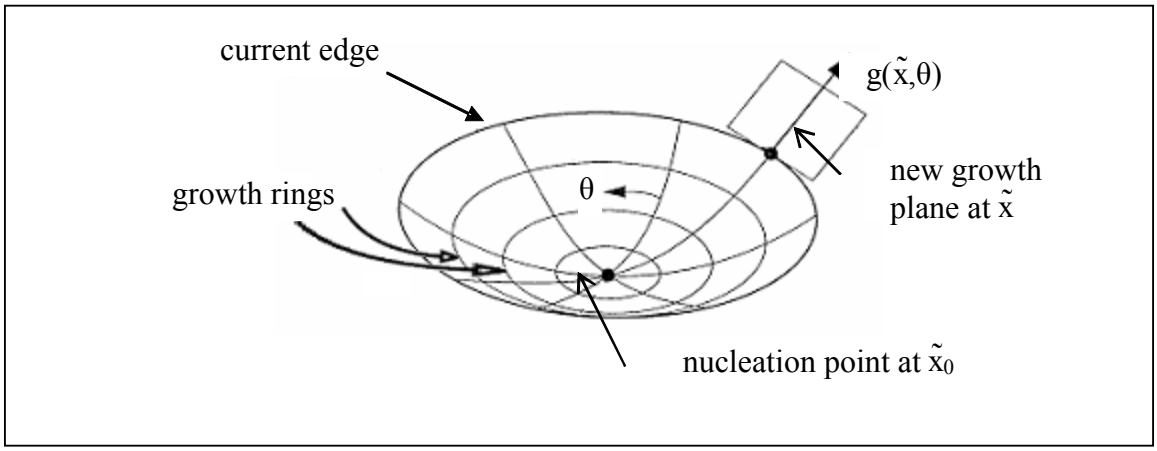

Source: Stewart Silling.

Figure 2. Shear band propagation model.

stops. However, the user has the option of turning the arrests off by setting an input flag. In that case, when the growth criteria are not met at points along the edge of the shear band, the band lies dormant until the growth criteria are satisfied at a later time. The yield stress of cells that contain the shear bands are reduced. Shear band nodes are convected with the material according to the local CTH cell face velocities.

3. Implementation of Schoenfeld-Wright Failure Criterion Into CTH

Initial assessment of the 3-D ASB model in CTH revealed that the band morphology was sensitive to user-specified nucleation and growth criteria. As a first step to reduce guess-work, a failure criterion by Schoenfeld and Wright (2003), based on earlier work by Wright (1992, 1994), is implemented into CTH to eliminate two of the nucleation criteria, namely user-specified thresholds for minimum strain and strain rate for nucleation. The criterion emphasizes homogenous behavior as defined by the material's constitutive response and does not require determination of any additional parameters experimentally.

In numerical implementation of the criterion, the peak stress in the adiabatic stress-strain curve that occurs at a fixed equivalent plastic strain is found for a given strain rate and flow law (Schoenfeld and Wright, 2003). Then the failure strain is estimated by multiplying a scale factor with the perturbation velocity, as indicated by the following expression:

$$\epsilon_{cr} - \epsilon_{max} = \sqrt{\left(-\frac{2m\sigma}{\pi \sigma_{,\epsilon\epsilon}} \right)_{max}} \; ln\left(\frac{1}{\beta}\right), \tag{7}$$

where ϵ_{cr} is effective failure strain, ϵ_{max} is effective strain that corresponds to peak stress in adiabatic response, subscript *max* indicates values at peak stress, σ is effective stress, $\sigma_{,\epsilon\epsilon}$ is

the curvature at the peak, and m is the strain rate sensitivity. Perturbation velocity, β, is interpreted as a variation in effective strain rate and can be calculated as follows:

$$\beta = \frac{\dot{\varepsilon} - \dot{\varepsilon}_{ave}}{\dot{\varepsilon}_{ave}}. \tag{8}$$

In a Lagrangian framework, the easiest approach to calculating the average strain rate for an element would be to use the strain rate values for neighboring elements. In the Eulerian context of CTH, the values at neighboring grid points may be used once the peak stress is reached at a grid point. However, the definition of the extent of the neighborhood that contributes to the average can be a complicated issue, and additional care must be taken so that the results are not mesh dependent. Various approaches to calculating the average are currently being investigated. The results presented in this report are obtained by including only the immediate neighboring grid points in the calculation. Furthermore, the strain rate values at the grid points on one of the three planes in z direction, called k-planes in CTH, correspond to a slightly earlier time than the other two planes included when calculating the average. This fact was known but ignored at the time the calculations reported herein were carried out. Modifications to CTH are planned to ensure that all strain rate values included in the average local strain rate calculation correspond to the same time, although changes in results are expected to be insignificant.

By employing the Schoenfeld-Wright failure criterion, for each strain rate observed in the flow field, a corresponding plastic strain value for failure is calculated based on the material model and used as a nucleation criterion. This not only reduces the guess work but also provides a more sensitive condition for nucleation. As demonstrated in section 4.2, the results obtained by employing the new physically-based failure criterion mimics experimental observations more closely, with much less effort by the user.

4. A Numerical Study: Steel Fragment Impact on Ti-6Al-4V Armor Plate

A series of experiments that involved a 20-mm fragment simulating projectile (FSP) impacting 28.58-mm thick Ti-6Al-4V extra-low interstitial (ELI) plates at a range of impact velocities were conducted at the U.S. Army Research Laboratory (ARL) in the late 90s (Burkins et al., 1997). Dimensions of the fragments used in the experiments are shown in figure 3. The primary objective of the experiments was to determine the effects of secondary heat treatment on ballistic limit velocity (V_{50}), the velocity at which a penetrator has 50% probability of perforating the target. It was observed that the ballistic performance and crater morphology of titanium alloys processed above β-transus and below β-transus differed drastically (Burkins et al., 1997)]. The dominant failure mechanism for the plates

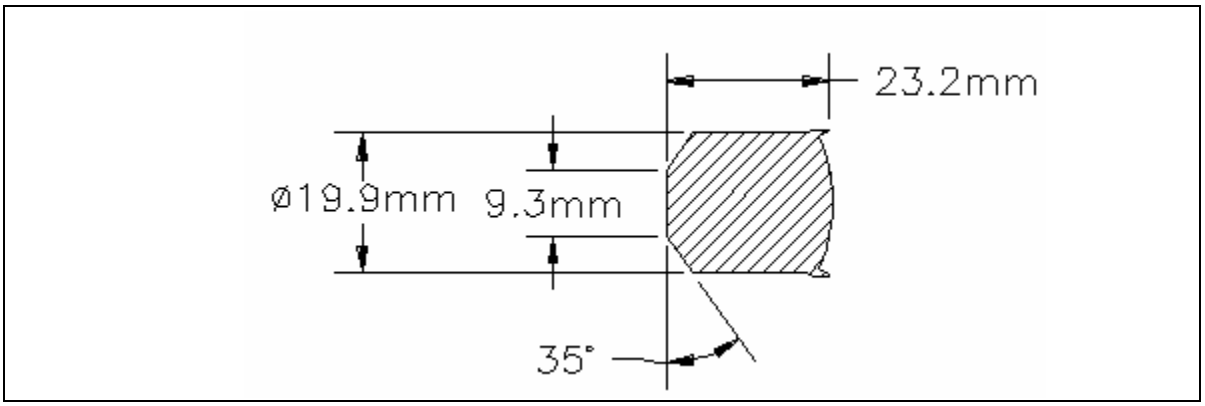

Figure 3. A 20-mm FSP (material–4340H steel; hardness–RC 29-31; nominal mass–54 g [Burkins et al., 1997]).

that were annealed below the β-transus temperature of 996 °C for this alloy was tensile spalling, with an approximate limit velocity of 1.1 km/s. On the other hand, the dominant failure mechanism for the plates that were annealed above the β-transus temperature was shear plugging, with a lower limit velocity of ~0.8 km/s. Shear bands were observed regardless of the annealing temperatures; however, they were more pronounced and visible for beta annealed plates, where the shear bands propagated through the entire thickness of the plate, parallel to the direction of impact, forming cylindrical plugs with very little bulging on the rear surface of the target (shown in figures 4b and 4c). For plates annealed below β-transus and for a vacuum creep flattened (VCF) plate, the ASBs propagated parallel to the direction of fire once again but were interrupted by delaminations in the rolling plane of the armor plate, perpendicular to the projectile path. These plates had much more pronounced bulging on the rear surface, along with cracks, as shown in figure 4a. Note that this discussion is based on 0° impact of Ti-6Al-4V (ELI) plates by 20 mm-FSPs only. Under different impact conditions, the ballistic ranking may be quite different (Weerasooriya et al., 2001).

A later study by Kad et al. (2002) numerically showed that the basal textures produced via rolling in the α-phase dominated microstructure (processed below β-transus) required a greater amount of work to drive localizations, compared to the transverse texture created by recrystallization above the β-transus temperature. For a detailed description of the anisotropic response of textured titanium alloy plates under ballistic conditions leading to shear plugging, refer to Kad et al. (2002).

In short, the morphology of ASBs in Ti-6Al-4V target plates due to ballistic impact, hence the ballistic performance of the titanium alloy, are experimentally observed to be sensitive to impact geometry and the plate microstructure. Not having an accurate representation of microstructural effects in the computational model, it is rather challenging to predict the dominant failure mode and ballistic limit velocity numerically.

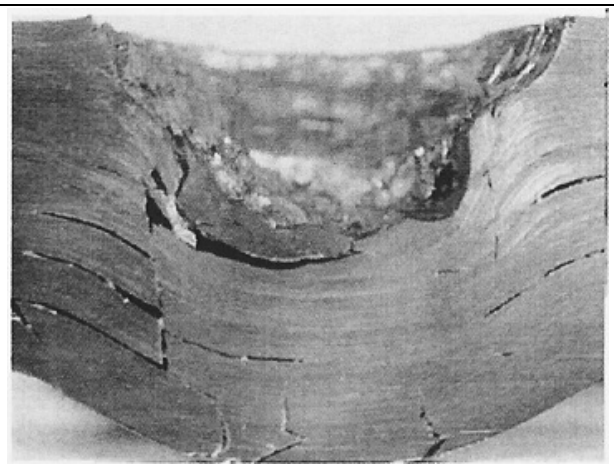

(a)

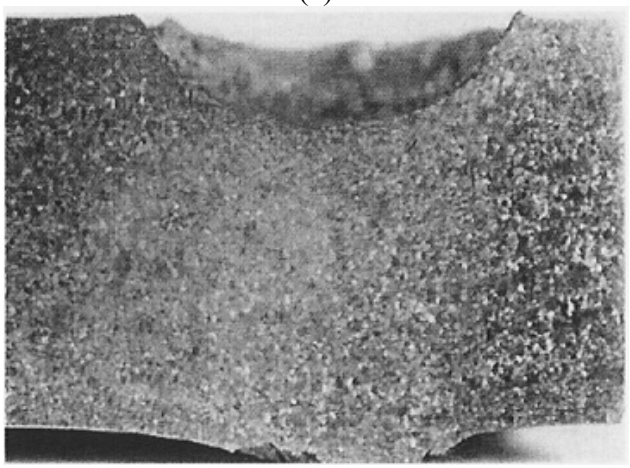

(b)

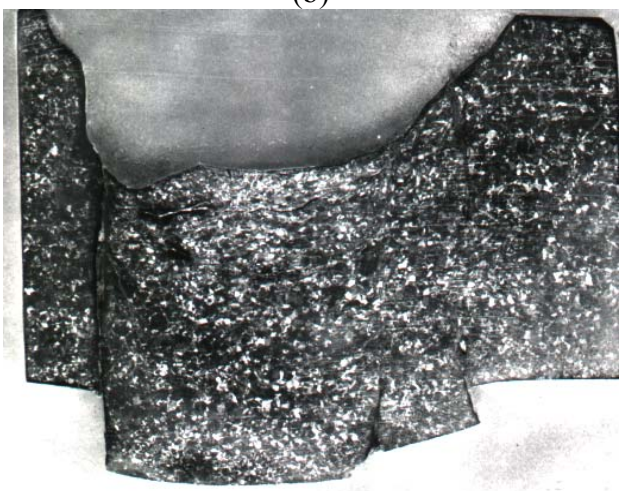

(c)

Source: M. Burkins.

Figure 4. Various failure modes in Ti-6Al-4V plates due to 20-mm FSP impact at 0°. (a) 23.5-mm thick VCF plate processed below β-transus and impacted at 1106 m/s; (b) 23.5-mm plate processed above β-transus and impacted at 813 m/s (Burkins et al., 1997); and (c) 38.1-mm plate processed above β-transus impacted at 1353 m/s.

4.1 Modeling Details

An initial 3-D configuration of CTH model that represents the fragment impact experiments conducted by Burkins et al. (1997) is shown in figure 5. The FSP is modeled as a homogeneous cylinder of 2-cm diameter and 2.32-cm length. The target plate is modeled as a 10- × 10-cm rectangular prism, with a thickness of 2.85 cm. The origin of the Cartesian coordinate system is at the center of the impact face of the cylinder. The x-axis is aligned with the axis of the cylinder and is positive in the direction of impact. The Mie-Grüneisen equation-of-state and Johnson-Cook constitutive model are used for both the projectile and the target materials, using the data available for low-cost (LC) Ti-6Al-4V processed below β-transus temperature, since material characterization data that correspond to (ELI) either above or below β-transus temperature were not available at the time this study was conducted.

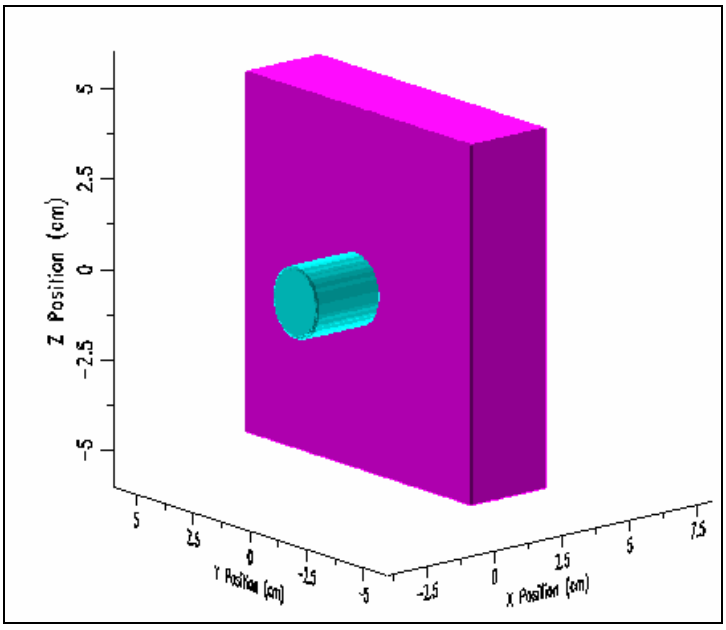

Figure 5. A 3-D CTH model for steel fragment impact on Ti-6Al-4V plate, at time = 0.

A 3-D rectangular mesh is used with 1-mm cubic cells. Hence, there are 20 cells across the diameter of the projectile. This mesh resolution may be viewed as more refined than a typical mesh to model this problem in CTH, but it is deemed adequate when the ASB model is activated. The model is not compatible with adaptive mesh refinement (AMR) at this time.

Input for shear band model should be included in the elastic-plastic input set, indicated by EPDATA keyword. To enable shear band nucleation and growth in a material, the SHEARBAND keyword should be entered for the material under the MATEP keyword. An example is provided as follows:

```
EPDATA
    VPSAVE          * must be used, because the shear band model uses plastic strain rate
    ...........
    ...........
    MATEP 1
        * select a constitutive model that computes equivalent plastic strain
        JO = 'STEEL'
        ..............
        ..............
        * allow shear bands in steel
        SHEARBAND
            SBEQPSNU      critical value
            SBEDOTNU      critical value
            SBDISTNU      critical value
            SBDISTAC      critical value
            SBEQPSGR      critical value
            SBEDOTGR      critical value
            SBVGROW       critical value
            SBNOARREST    value
            SBNUCCOND     value
ENDE
```

If shear bands are not to be allowed in a material, the SHEARBAND keyword is simply not included.

4.2 Numerical Results

A list of shear band input criteria used in the numerical simulations presented in this section is provided in table 1. If the nucleation condition listed in table 1 is 0, nucleation is not allowed to occur in mixed cells; if it is 1, nucleation is allowed to occur only in mixed cells; and if it is 2, it can occur regardless of whether or not the candidate cell for nucleation is mixed. S-W indicates that the Schoenfeld-Wright failure criterion is used instead of the user-specified nucleation criteria for strain and strain rate. W-O indicates Wright-Ockendon length scale. As indicated in table 1, shear bands were allowed to be arrested in each of the cases discussed in this section.

Using the Johnson-Cook constitutive model for a range of strain-rates between 100 and 5,000,000, values of strain that correspond to peak stress for the LC Ti-6Al-4V vary between 0.2575 and 0.2175. Prior to the implementation of the Schoenfeld-Wright critierion into CTH and since only a single value of strain rate and strain is selected by the user, 10,000 is chosen to be a representative strain rate for the range. The corresponding value of strain at peak stress for this strain rate is ~0.24. Hence, 0.25 is selected to be the critical value for ASB nucleation, as listed in table 1. To prevent a large number of nucleations without any

Table 1. Summary of user-specified shear band criteria used to obtain numerical results shown in figures 8–13 and 14–17.

Value	Keyword	Description	Figure				Units
			8–13	14	15, 16	17	
ε_{cr}^{nu}	SBEQPSNU	Critical equivalent plastic strain for nucleation.	0.25	0.25	S-W	S-W	None
$\dot{\varepsilon}_{cr}^{nu}$	SBEDOTNU	Critical plastic strain rate for nucleation.	1.0e4	1.0e4	S-W	S-W	s^{-1}
D_{cr}	SBDISTNU	Minimum distance to other shear bands at time of nucleation.	1	1	1	1 to W-O	cm
D_{cr}^{*}	SBDISTAC	Minimum distance to active shear bands at time of nucleation.	1	1	1	1 to W-O	cm
ε_{cr}^{gr}	SBEQPSGR	Critical equivalent plastic strain for growth.	0.05	0.05	0.05	0.05	None
$\dot{\varepsilon}_{cr}^{gr}$	SBEDOTGR	Critical plastic strain rate for growth.	1.0e2	1.0e2	1.0e2	1.0e2	s^{-1}
V	SBVGROW	Growth speed; if 0, bands advance one mean cell width per time step.	0	0	0	0	cm/s
	SBNOARREST	Flag for shear band arrest: = 0 ... arrested. = 1 ... not arrested.	0	0	0	0	None
	SBNUCCOND	nucleation condition: = 0 ... never on material interfaces or free surfaces. = 1 ... only on material interfaces and free surfaces. = 2 ... anywhere.	0	2	2	2	None

propagation, the user-specified critical values for ASB growth needed to be less than their counterparts for nucleation. As a result of several numerical tests, the smallest strain rate in the range originally considered (i.e., 100) and 1/5th of the critical value of nucleation strain are chosen to be the growth criteria. As listed in table 1, after the implementation of the Schoenfeld-Wright criterion, the nucleation criteria is replaced. However, the growth criteria are kept the same to provide one-to-one comparison. Various options to eliminate user-specified growth criteria is currently being investigated.

Unless otherwise noted, the impact speed for the numerical simulations is chosen to be the ballistic limit velocity indicated in experiments conducted by Burkins et al. (1997) (i.e., 1.1 km/s) since at this speed, shear bands were observed for the ELI plate of 28.58-mm thickness. Although the dominant failure mode is not plugging under the conditions studied, shear bands are expected to propagate towards the back of the target attempting to form a plug in this numerical study since the additional failure mechanism of in-plane delaminations that absorb the kinetic energy of the projectile and interrupt shear band propagation, is not modeled. V_{50} for LC Ti-6Al-4V, processed below β-transus temperature and corresponding to 20-mm FSP 0º impact on a 25.35-mm plate, is 1.016 km/s (Burkins et al., 2001). Slightly lower ballistic limit velocity is observed for a slightly thinner plate. A cut-out section of the LC plate was not available at the time this report was written and, hence, could not be

included in this report to provide a comparison for ASB morphology observed numerically. However, the back surface of the LC plate is shown in figure 6 and will be discussed later in this section.

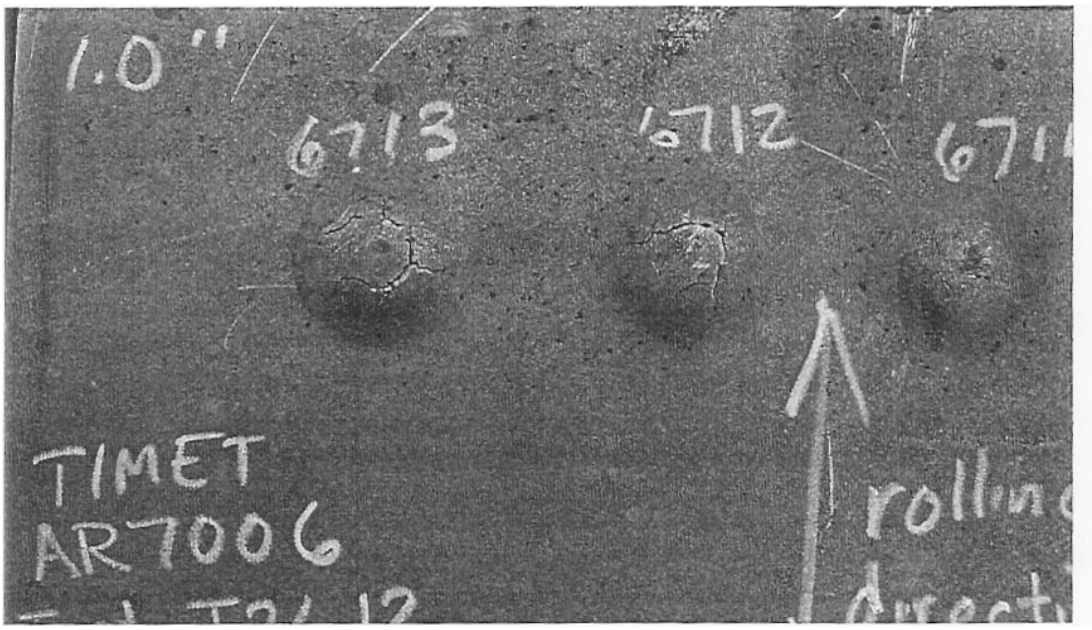

Figure 6. Photograph of the rear surface of a 24.64-mm thick Ti-6Al-4V (LC) plate (Burkins et al., 2001).

The current distribution of CTH, not having shear localization capability, cannot predict plugging type of failure, as indicated in figure 7. At 70 μs and at the end of the penetration process, only a small bulge in the back of the target is visible. In this case, the fracture model is turned off to merely observe the effect of activating the shear band model.

When shear bands are allowed to form in the titanium alloy, they propagate toward the back of the target along planes of maximum shear, attempting to form a plug, resulting in a distinctive protrusion seen in the back of the target (figure 8). Figure 9 shows the corresponding shear band formations, both in 2-D on a cut-out section of the plane of symmetry, and also in 3-D, at various times during the penetration process. Note that the shear bands that develop at a later stage propagate in a spiral manner in the 3-D figures. A total of six shear bands nucleated during this simulation: four at 2.4 μs, one at 5.8 μs, and one at 18.4 μs. All six shear bands were inactive past 22 μs. The color of the shear bands displayed in the 2-D images on the left side in figure 9 provides a hint to the order of nucleation as follows: dark blue for shear band 1, blue for shear band 2, dark green for shear band 3, green for shear band 4, light green for shear band 5, and yellow for shear band 6. However, it should be clarified here that in the current version of the model, since more than one shear band could occupy the same cell, shear bands and therefore the colors that

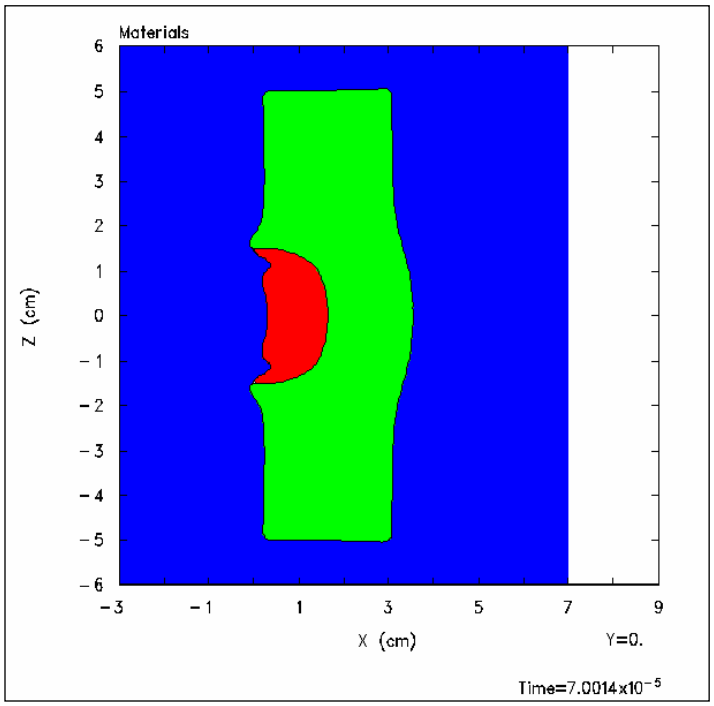

Figure 7. FSP impact on Ti-6Al-4V plate. Result obtained by deactivating the shear band model (time = 70 μs, and impact velocity = 1.1 km/s).

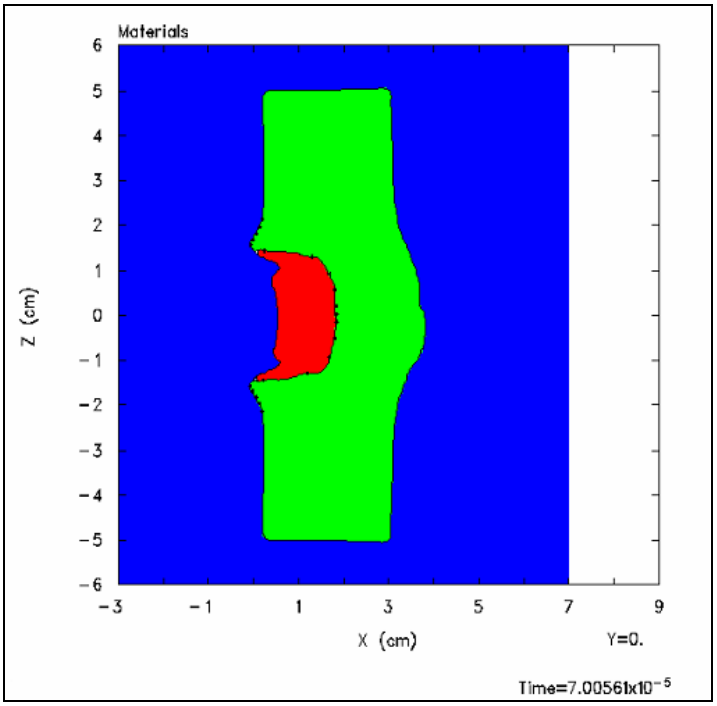

Figure 8. FSP impact on Ti-6Al-4V plate. ASB model activated with user-specified critical plastic strain and strain rate for nucleation (time = 70 μs, and impact velocity = 1.1 km/s).

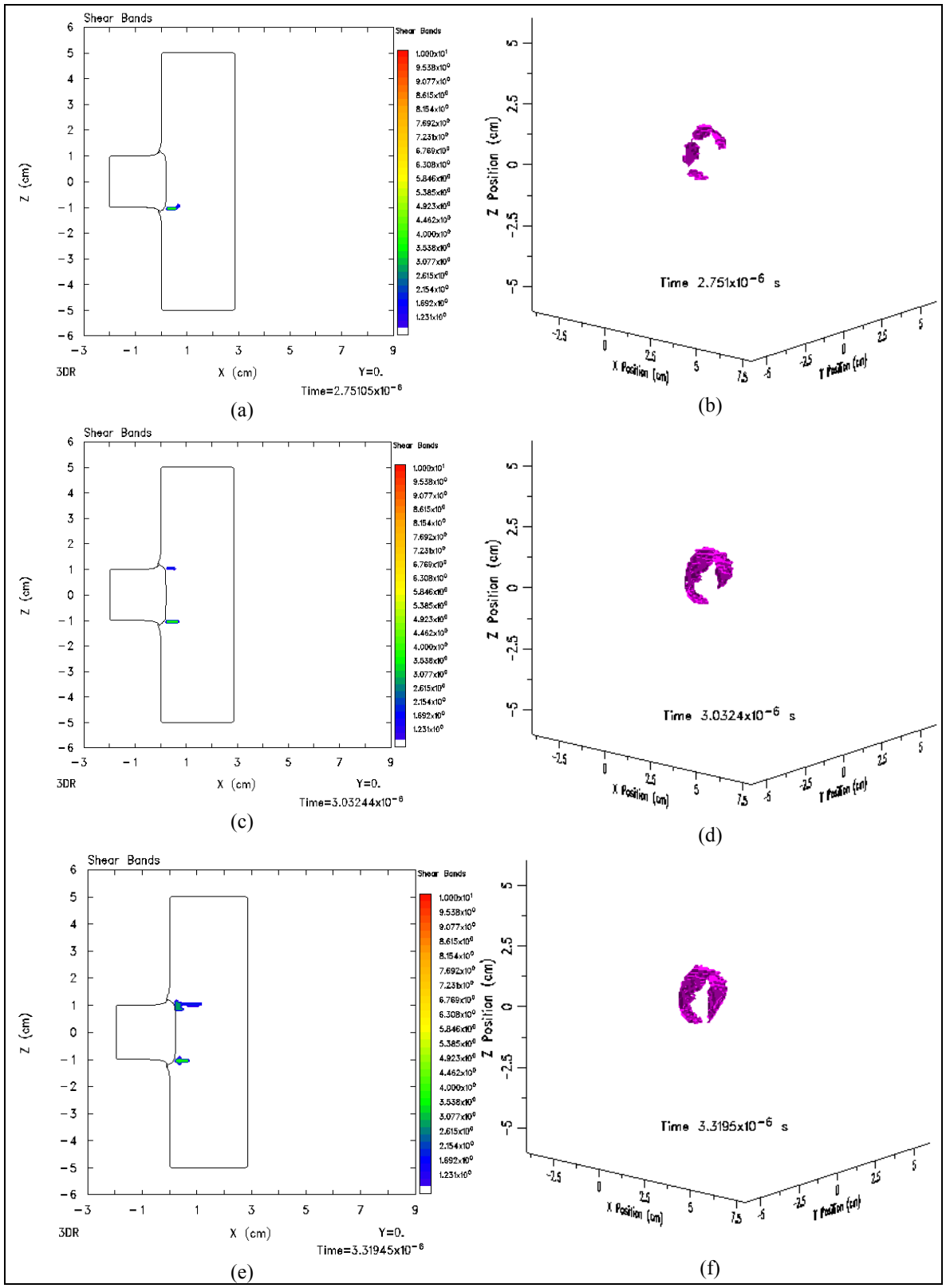

Figure 9. ASB model activated with user-specified critical plastic strain and strain rate for nucleation (impact velocity = 1.1 km/s). Shear band nucleation and propagation on x-z plane and in 3-D.

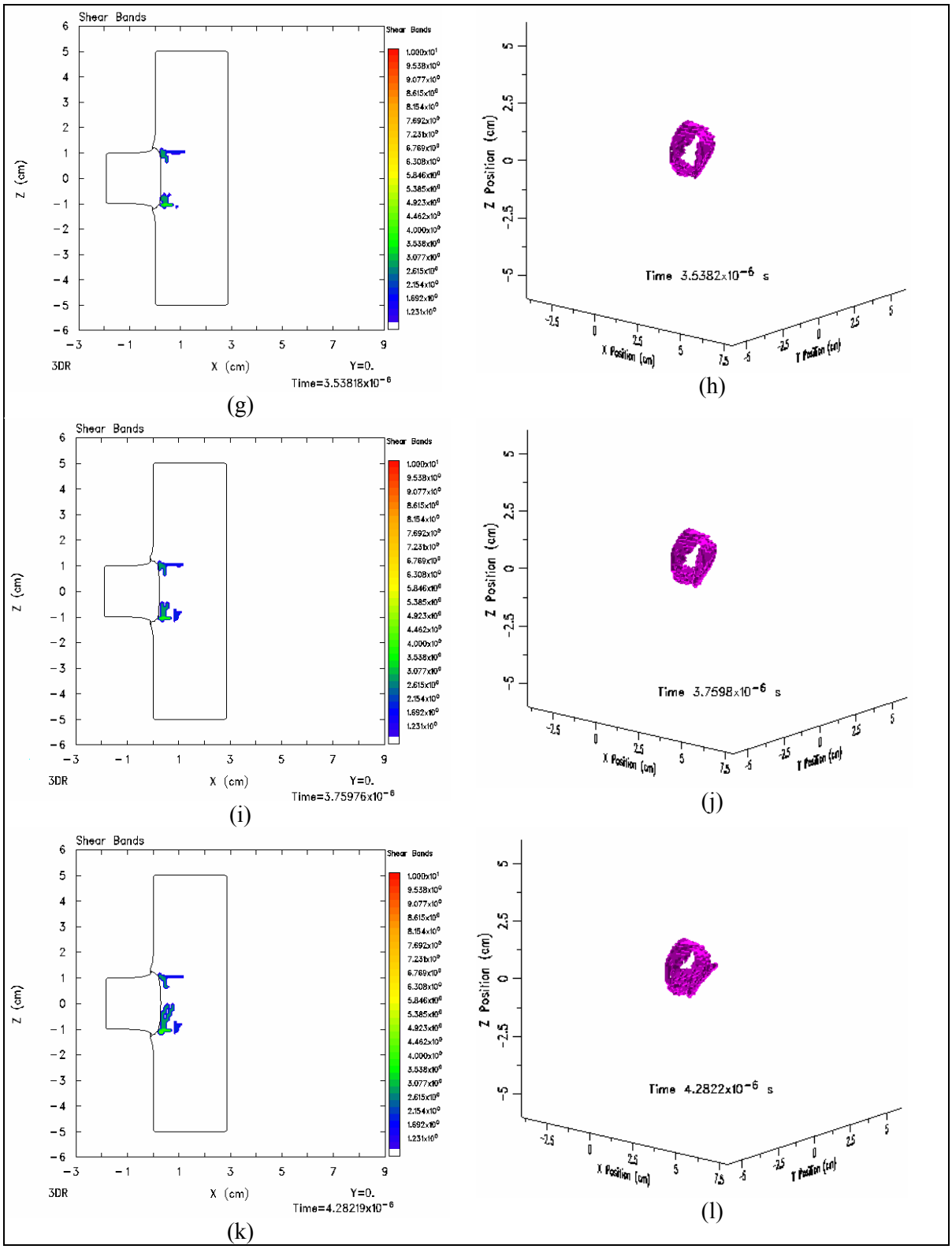

Figure 9. ASB model activated with user-specified critical plastic strain and strain rate for nucleation (impact velocity = 1.1 km/s). Shear band nucleation and propagation on x-z plane and in 3-D (continued).

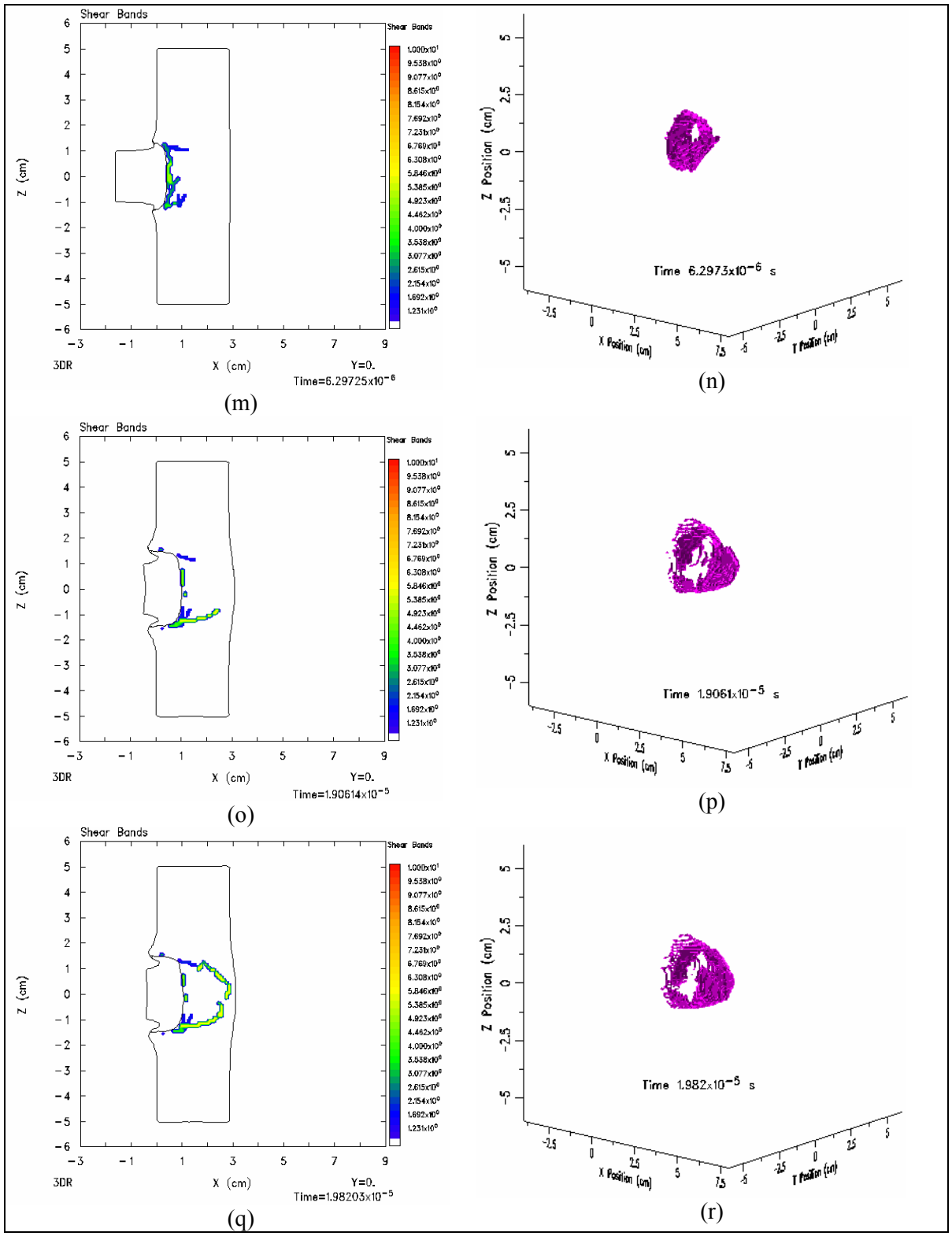

Figure 9. ASB model activated with user-specified critical plastic strain and strain rate for nucleation (impact velocity = 1.1 km/s). Shear band nucleation and propagation on x-z plane and in 3-D (continued).

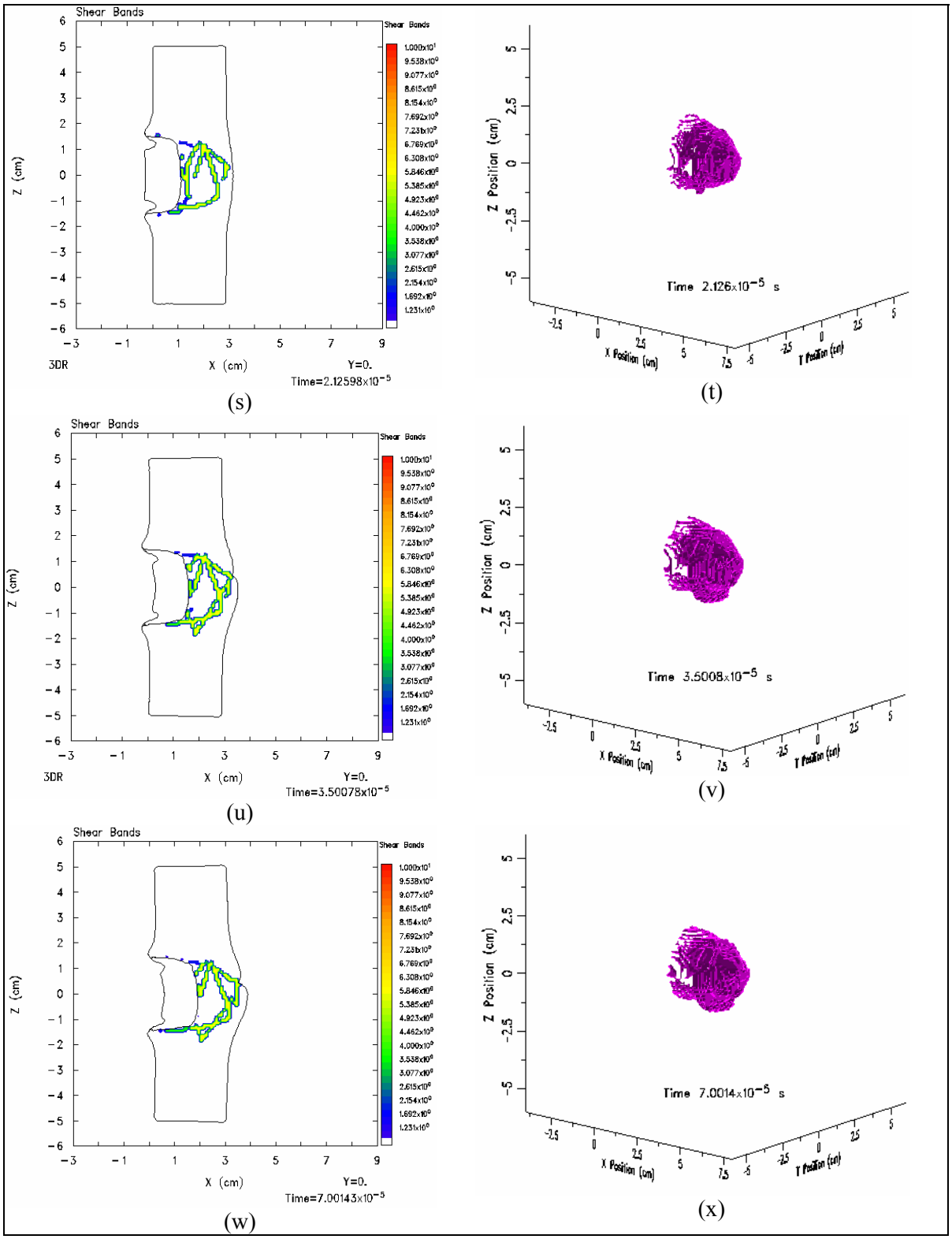

Figure 9. ASB model activated with user-specified critical plastic strain and strain rate for nucleation (impact velocity = 1.1 km/s). Shear band nucleation and propagation on x-z plane and in 3-D (continued).

represent them may be overlapping. It is planned to limit one nucleation per cell in the future.

Figures 10–12 show the corresponding equivalent plastic strain, strain rate, and velocity, respectively at 2, 3, 5, 6, 18, and 25 μs, in accordance with shear band nucleation times. In other words, each row represents a state that precedes and follows a shear band nucleation.

Without the ASB model, the ballistic limit velocity for this problem cannot be predicted using the current distribution of CTH. Although the results presented thus far seem promising, the prediction of the ballistic limit velocity is still rather difficult, even when the ASB model is activated. Some of the reasons for this difficulty are as follows:

1. Additional failure mechanisms that influence the dominant failure mode and the ballistic limit velocity, such as in-plane delamination and microstructure effects, are not modeled.
2. The propagation velocity of shear bands is not yet properly modeled.
3. User-specified criteria influence the morphology of shear bands and consequently the dominant failure mode and ballistic limit velocity.

However, the results presented thus far indicate a plug about to be formed and may be taken as representative of a state of an armor plate impacted at ballistic limit velocity. Taking this state as a basis, four other velocities were tested to investigate if shear band nucleation and propagation will be consistent with increasing impact velocity and determine if a plug will actually be formed at higher impact velocities. The velocities tested were 900, 1000, 1200, and 1300 m/s. Approaching from below the ballistic limit produced expected results, i.e., the shear band propagation did not reach the back of the target for 0.9- and 1-km/s impact speeds. In general, more shear bands were generated as the impact velocity increased from 900 to 1300 m/s; five shear bands for 900 m/s; six shear bands for 1000 and 1100 m/s; seven shear bands for 1200 m/s; and eight shear bands for 1300 m/s. However, once past the ballistic limit, the plug formation was not complete at the end of the penetration process, as anticipated. A more defined protrusion in the back of the target was produced at 1.2 km/s. At 1.3 km/s, the generated shear bands became distorted once inactive, since a plug could not be formed. The rear surface of the target lost the definitive plug shape observed for impact speeds 1.1 and 1.2 and was simply a more pronounced bulge than the one observed in figure 7. These results prompted an investigation, which is still underway, to determine the cause. The material response on the back surface of the target for three different velocities is shown in figure 13.

The rear surface of a 24.64-mm thick Ti-6Al-4V LC plate impacted by a 20-mm FSP at various impact speeds is shown in figure 6. The impact speeds for shots 6711, 6712, and

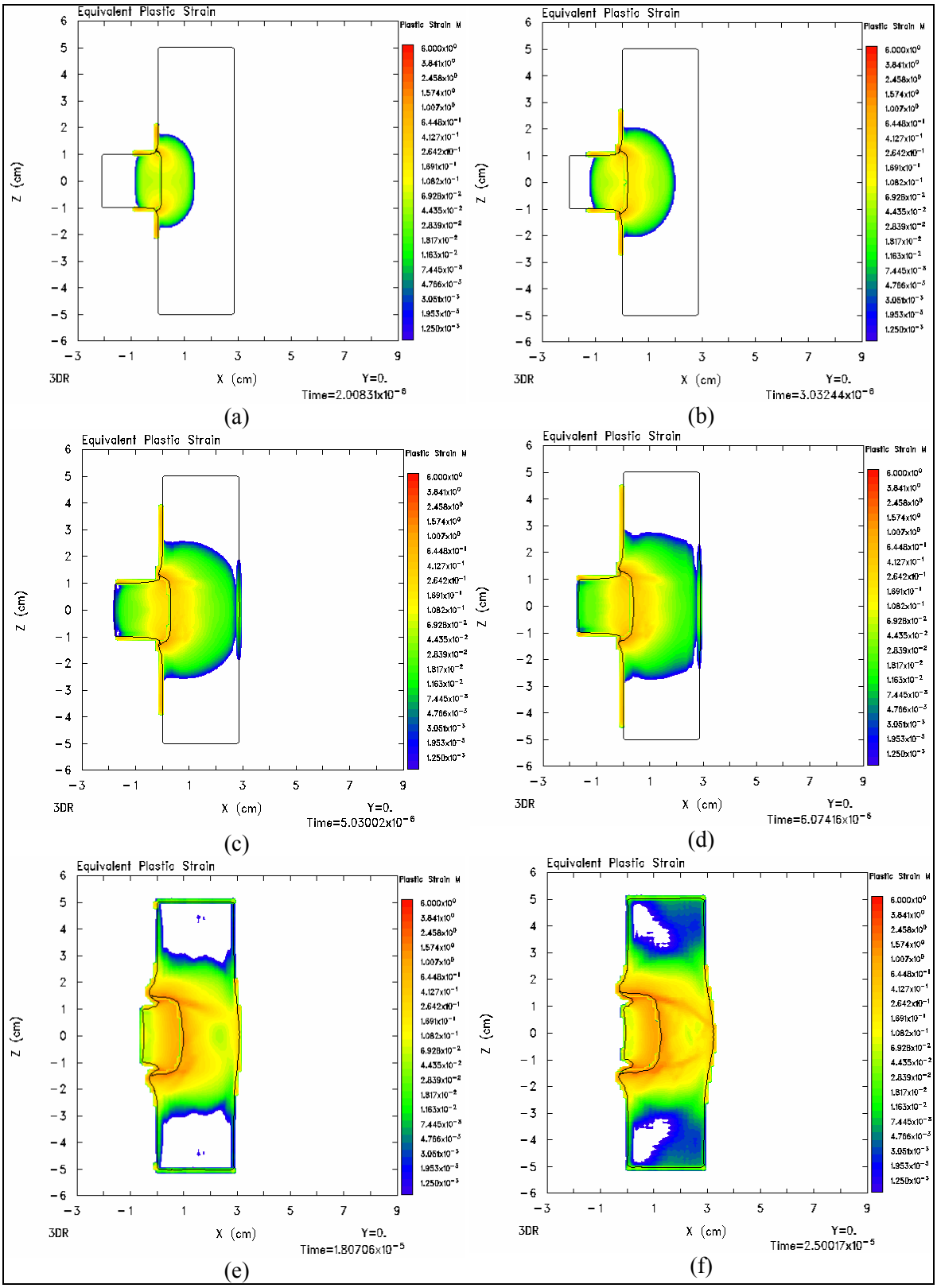

Figure 10. ASB model activated with user-specified critical plastic strain and strain rate for nucleation (impact velocity = 1.1 km/s). Equivalent plastic strain at various times.

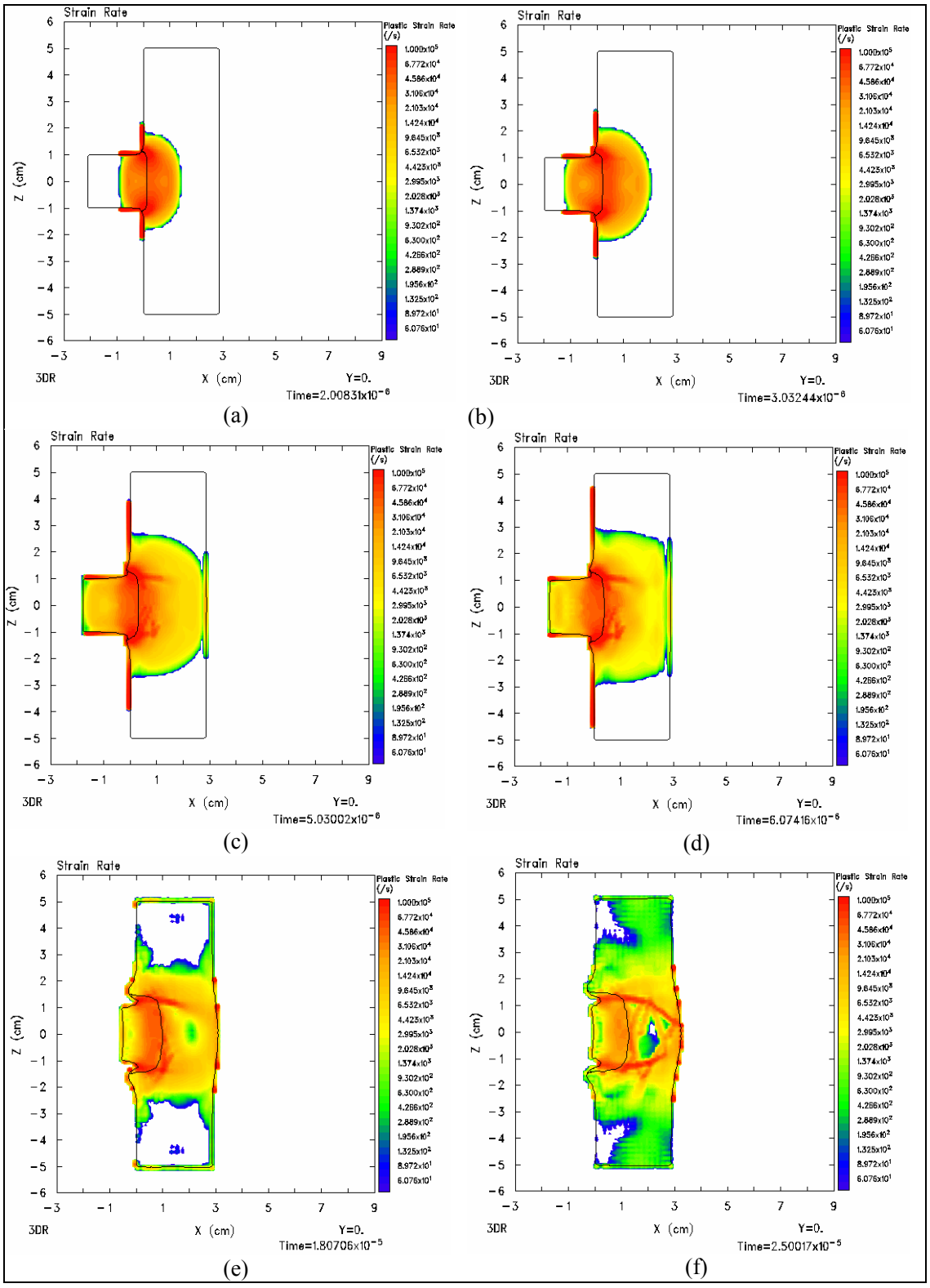

Figure 11. ASB model activated with user-specified critical plastic strain and strain rate for nucleation (impact velocity = 1.1 km/s). Strain rate at various times.

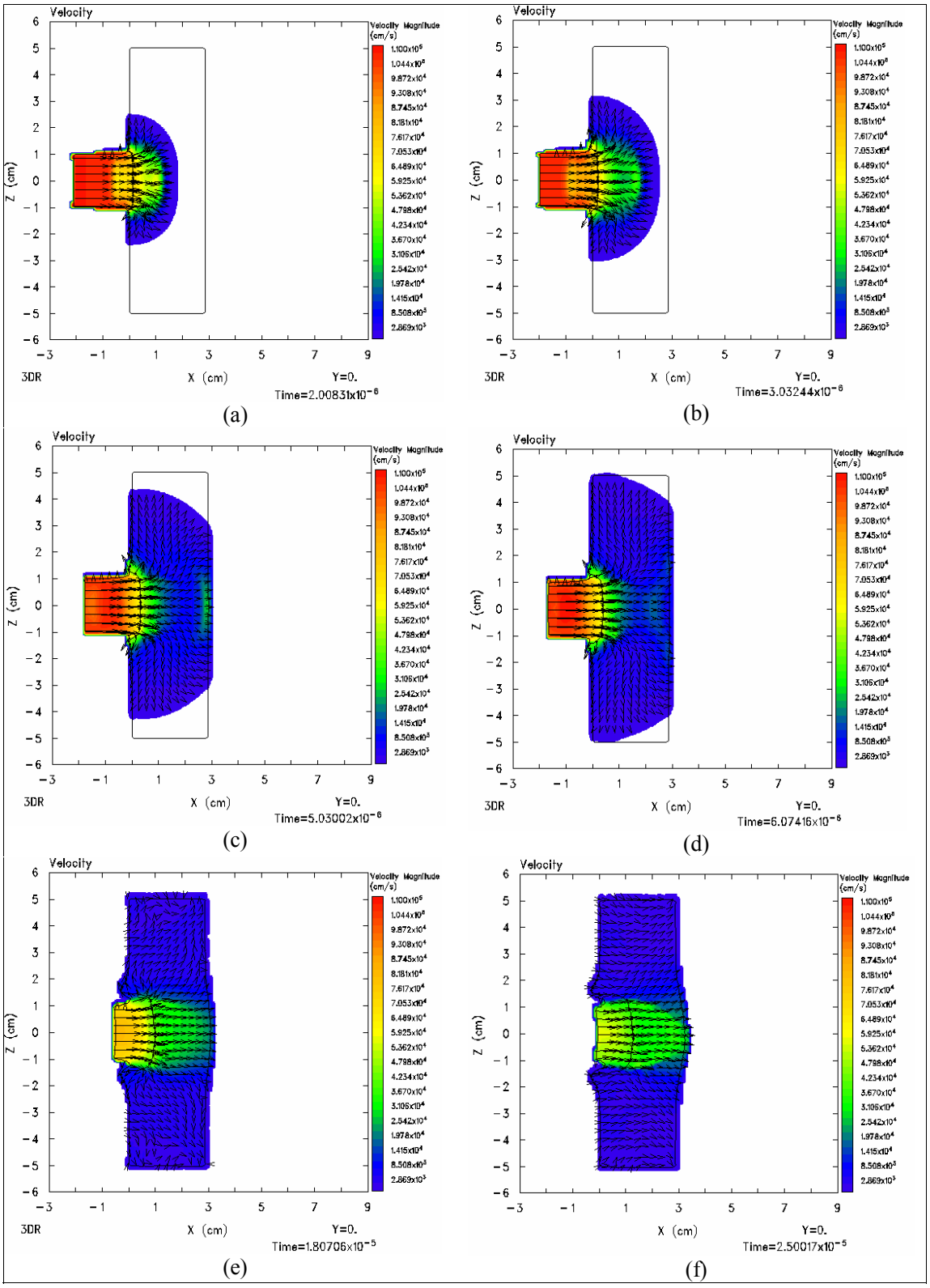

Figure 12. ASB model activated with user-specified critical plastic strain and strain rate for nucleation (impact velocity = 1.1 km/s). Velocity magnitude at various times.

6713 seen in the photograph are 947, 984, and 1008 m/s. All the shots shown bulged between 5 and 7 mm, and cracks are visible. Note that the plate shown in the photograph is thinner than the 25.85-mm plate modeled, and the impact velocities for shots shown in the photograph are lower than the impact velocity numerically studied, which is 1100 m/s.

Considering this fact and also taking into consideration that the ASB propagation speed was controlled by the mesh size currently, the ASB model in CTH was found to be quite promising in predicting ballistic limit velocity, even at its current stage (see figures 13 and 6).

In Silling's earlier 2-D shear band model, nucleation was allowed only on material boundaries and free surfaces, since the model was only designed to study the self-sharpening effect in penetrators. The results displayed in figures 8–13 were obtained by not allowing shear bands to nucleate along material boundaries and free surfaces, per Silling's 3-D ASB model. In order to study the effect of nucleation sites on shear band morphology, another input parameter was added to the ASB model, as described in section 2. With the same input set used to create figures 8–13 and employing the new input parameter, the nucleation requirement was cancelled (i.e., no preference was made as to whether or not nucleations occurred on material boundaries or free surfaces). Resulting images corresponding to the end of the penetration process, i.e., at 70 μs, are shown in figure 14. Note that the band morphology has changed, yet the overall effect of activating the ASB model remained the same (i.e., the shear bands still propagated and reached the back of the target, attempting to form a plug). In addition, the band formations were closer to experimental observations.

Several different combinations of input criteria for nucleation and growth of shear bands were tested. Even though the global effect did not change for reasonable combinations of parameters, the formations of shear bands differed in each case. Hence, reducing the ambiguity in selecting the input parameters was imperative. As a step in this direction, the Schoenfeld-Wright criterion based on ideas developed by T. Wright (1992, 1994) was implemented into CTH and effectively eliminated two of the user-specified criteria, as discussed next.

When the Schoenfeld-Wright criterion was applied to replace the user-specified criteria for nucleation strain and strain rate, the results shown in figure 15, compared to figure 14, were obtained. The first four shear bands nucleate symmetrically around the impact area within the first couple of microseconds after the impact. They cannot be seen in the 2-D images in figures 15 and 16, since they are not on the x-y plane shown. The fifth shear band appears at 12 μs, ahead of the penetrator tip, and the other two shear bands that reach the back of the target nucleate at 29.3 μs, when the fragment is proceeding inside the target with an approximate velocity of only 250 m/s. They propagate in a spiral pattern, as shown by the 3-D growth sequence in figure 16. The results shown in figures 15 and 16 revealed that further improvements can be made to improve the computational outcome. Nevertheless,

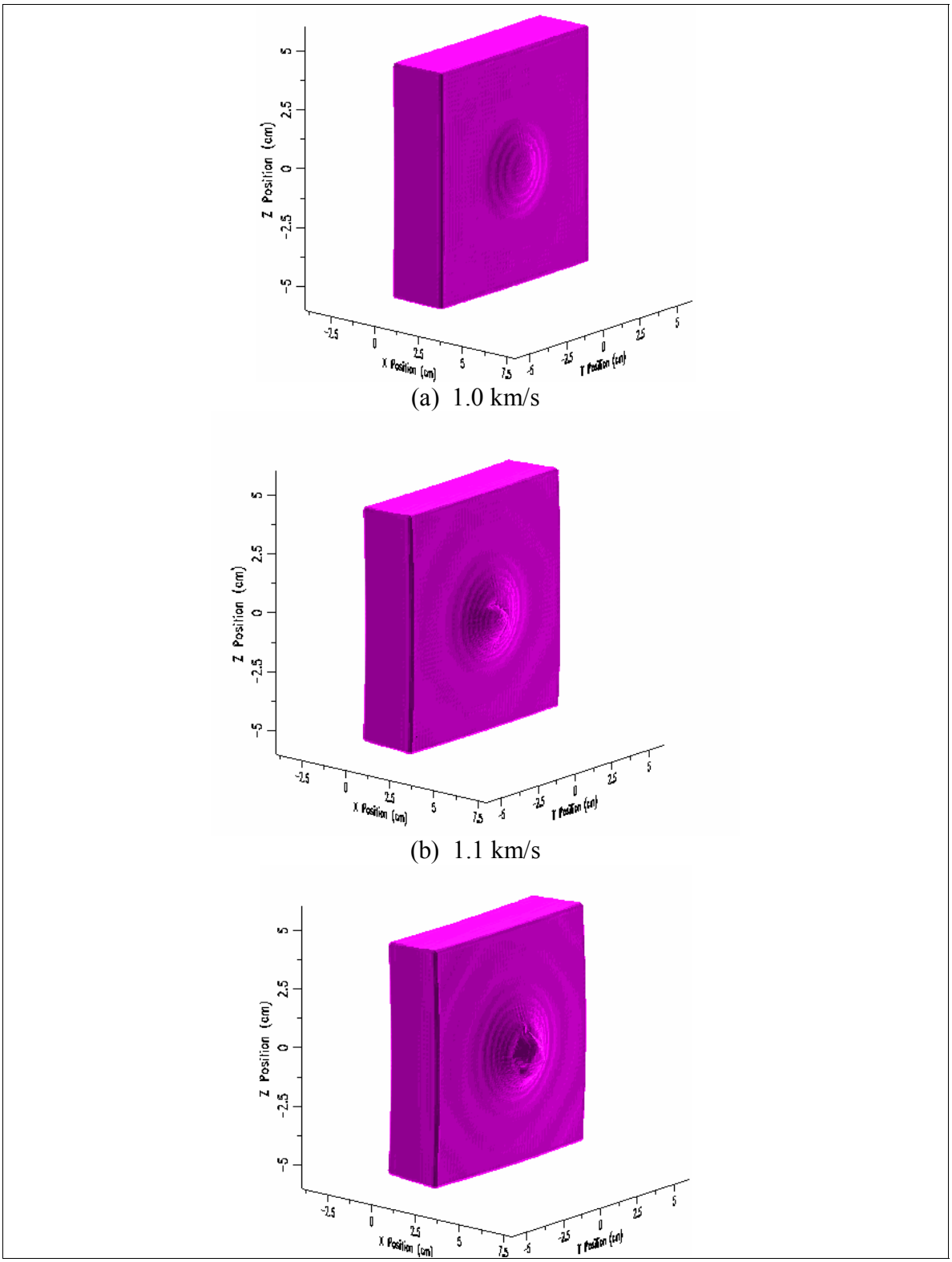

(a) 1.0 km/s

(b) 1.1 km/s

Figure 13. Steel fragment impact on Ti-6Al-4V armor plate. Material response on the rear surface of the target plate for three different impact velocities.

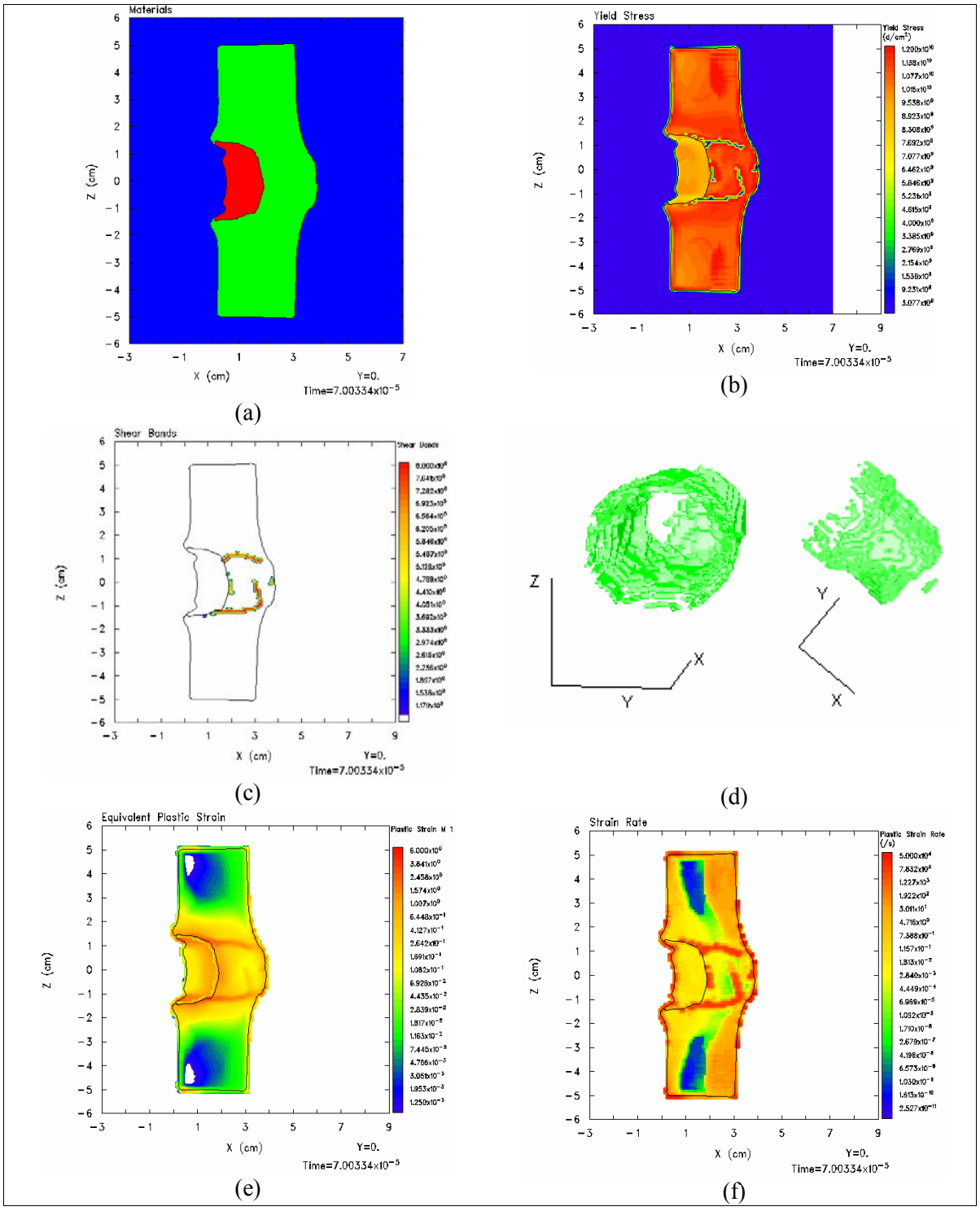

Figure 14. ASB model activated with user-specified nucleation criteria. No preference on nucleation locations (impact speed = 1.1 km/s). Results shown at 70 μs.

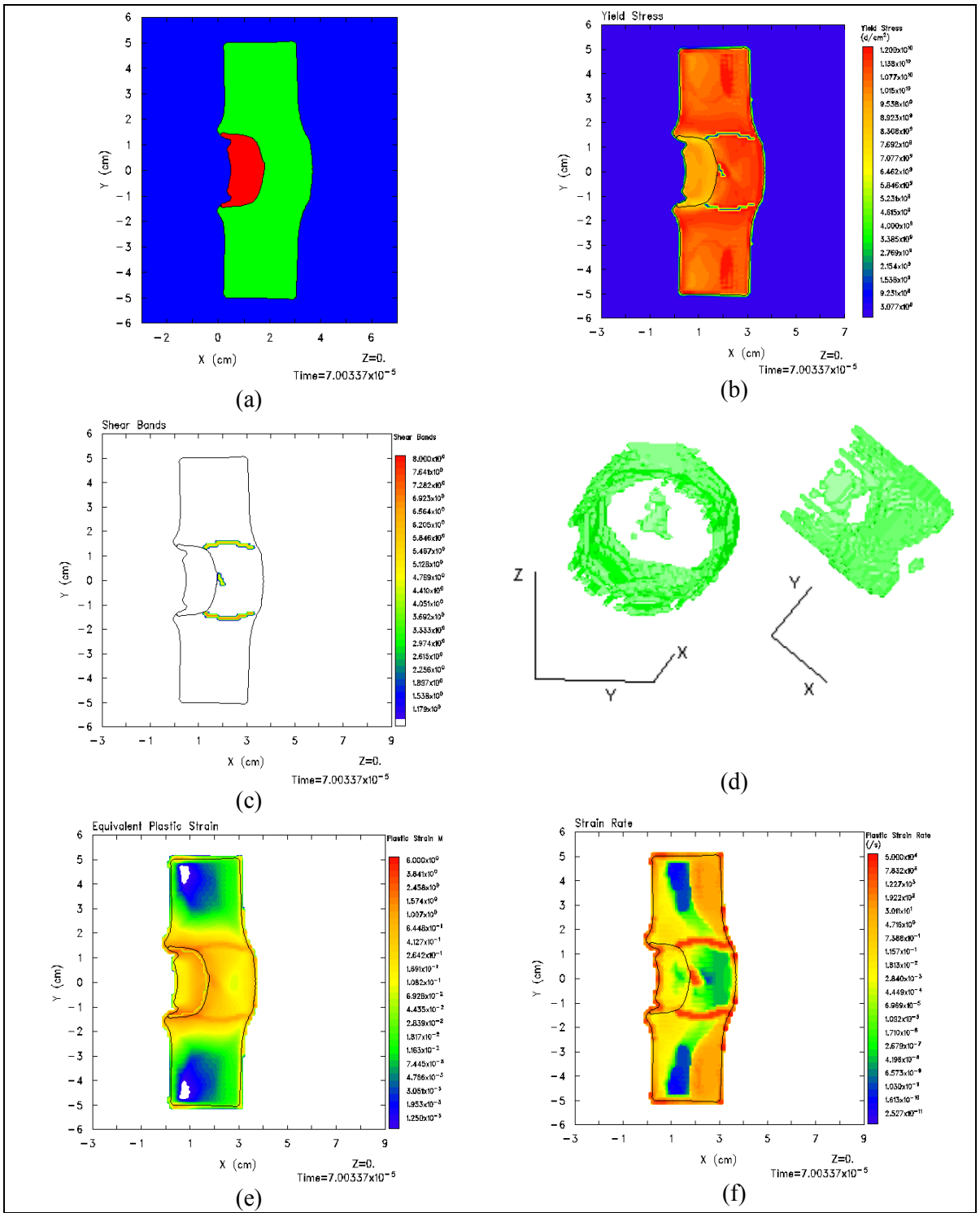

Figure 15. ASB model activated along with Schoenfeld-Wright criterion. No preference on nucleation locations (impact speed = 1.1 km/s). Results shown at 70 μs.

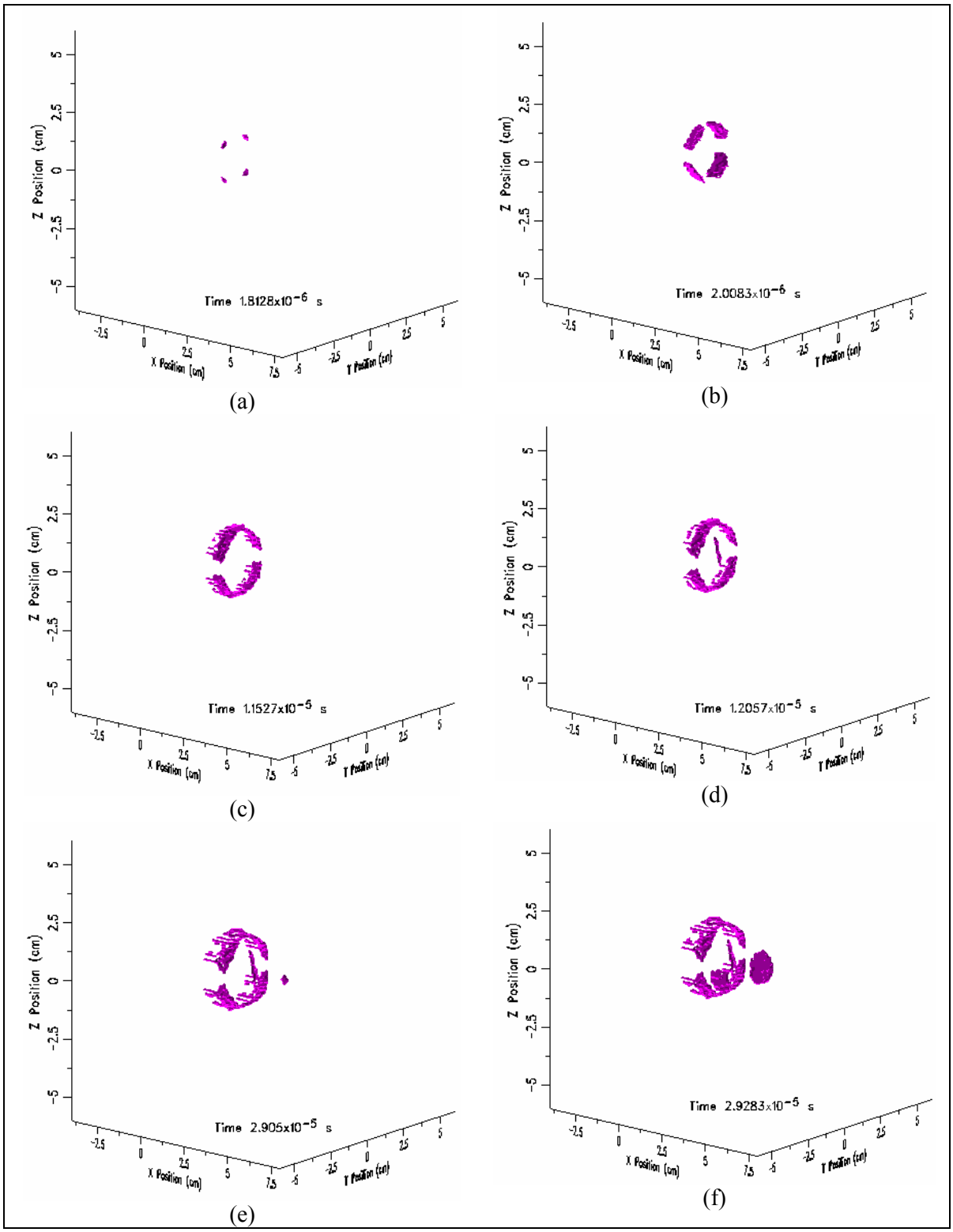

Figure 16. Shear band nucleation and propagation sequence due to steel fragment impact on Ti-6Al-4V plate using Schoenfeld-Wright criterion. No preference on nucleation locations (impact speed = 1.1 km/s). Results shown at 70 μs.

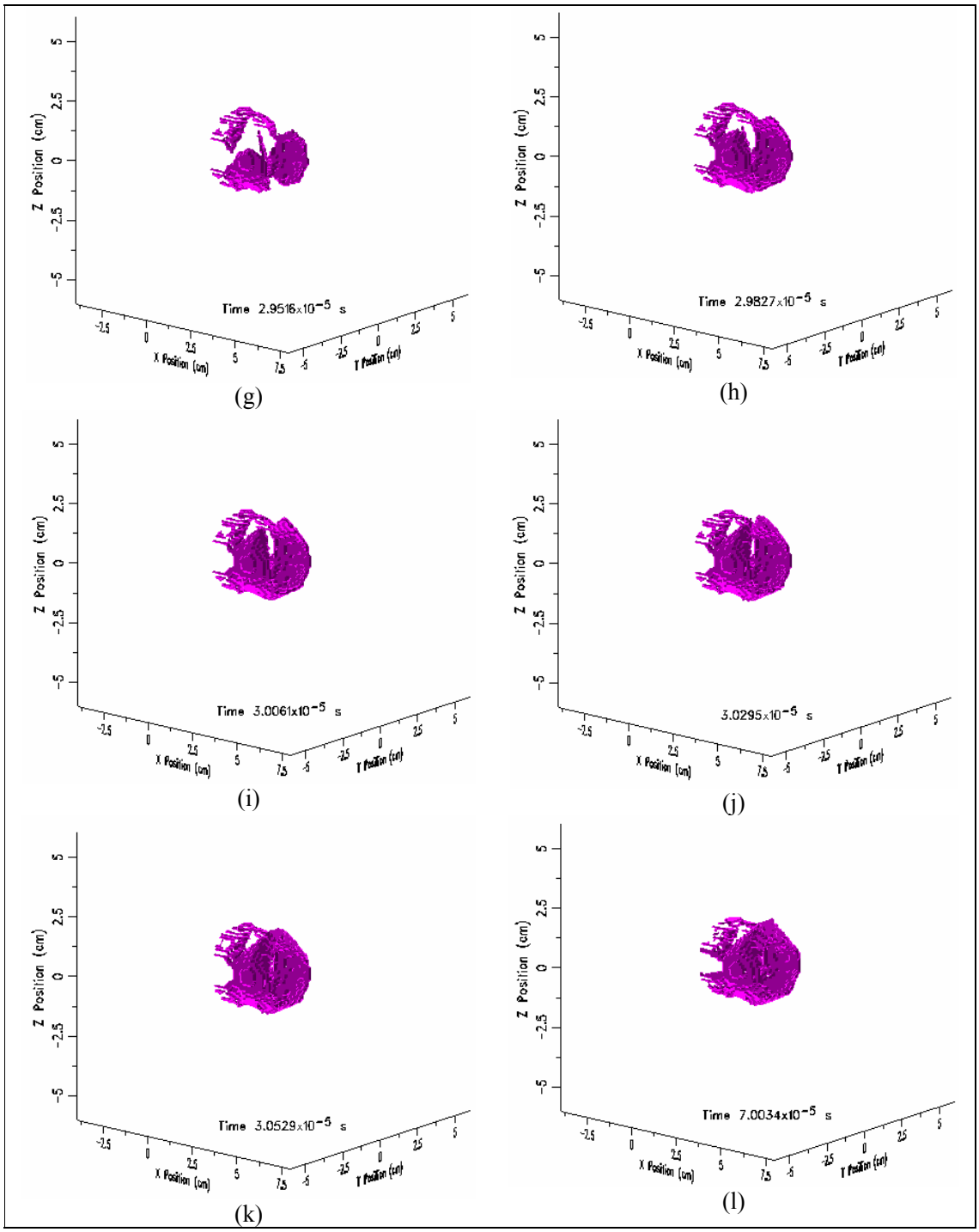

Figure 16. Shear band nucleation and propagation sequence due to steel fragment impact on Ti-6Al-4V plate using Schoenfeld-Wright criterion. No preference on nucleation locations (impact speed = 1.1 km/s). Results shown at 70 μs (continued).

they are included in this report to provide insight into the direct influence of applying the Schoenfeld-Wright criterion when all the other criteria are kept the same.

Once the trial-error process in setting a critical value for nucleation strain and strain rate is eliminated, it is now possible to study the effects of assigned shear band spacing more exclusively, although there are still other criteria and conditions that effect the solution. In order to investigate the effects of required shear band spacing, the minimum distance to other active or inactive shear bands is gradually decreased by 1 mm at a time, starting with 1 cm on the higher end and the Wright-Ockendon length scale (Nesterenko et al., 1998) on the lower end. Figures 15 and 16 correspond to the higher end (i.e., 1-cm requirement). The effect of gradually decreasing the minimum distance requirement is shown in figure 17.

The capability to calculate and utilize the Wright-Ockendon and Grady-Kipp length scales was added to the ASB model, and the Wright-Ockendon length scale was used in order to obtain the results shown in figure 17i. Once the peak stress was reached in the adiabatic stress-strain curve, at each location where the Schoenfeld-Wright criterion was satisfied, the Wright-Ockendon length scale was calculated using the local values of parameters in the following equation:

$$L_{W-O} = 2\pi \left[\frac{kC_v m^3 \dot{\gamma}_0^m}{\dot{\gamma}^{(3+m)} a^2 \tau_0} \right]^{1/4}, \tag{9}$$

where k is the heat conduction coefficient, m is the strain rate sensitivity, a is thermal softening parameter used in the constitutive model, and τ_0 is the flow stress at reference temperature. Note that when the Wright-Ockendon length scale is used, the heat conduction section has to be included in the CTH input deck. For the calculation presented in this report, room temperature value was used for the titanium alloy conduction coefficient, since accurate and detailed thermal properties were not available. The Grady-Kipp length scale is ~12.5× the Wright-Ockendon length scale and is therefore rather large for the geometric dimensions of this problem, based on the results obtained for 1-cm spacing. On the other hand, the Wright-Ockendon length scale is quite small, and the minimum distance requirement is rather relaxed in comparison. As a result, the maximum number of shear bands currently allowed to nucleate, 100 at the time these computations were carried out, is reached within the first 2.3 μs. No other shear bands could nucleate after that time, even if the other conditions for nucleation were satisfied. This case revealed a minor inefficiency in the algorithm—that the number of nucleations per cell are not limited currently—which results in excessive shear band nucleations when the distance requirement is sufficiently small. To prevent this problem, adding a limitation on the number of shear band nucleations allowed in each cell is planned.

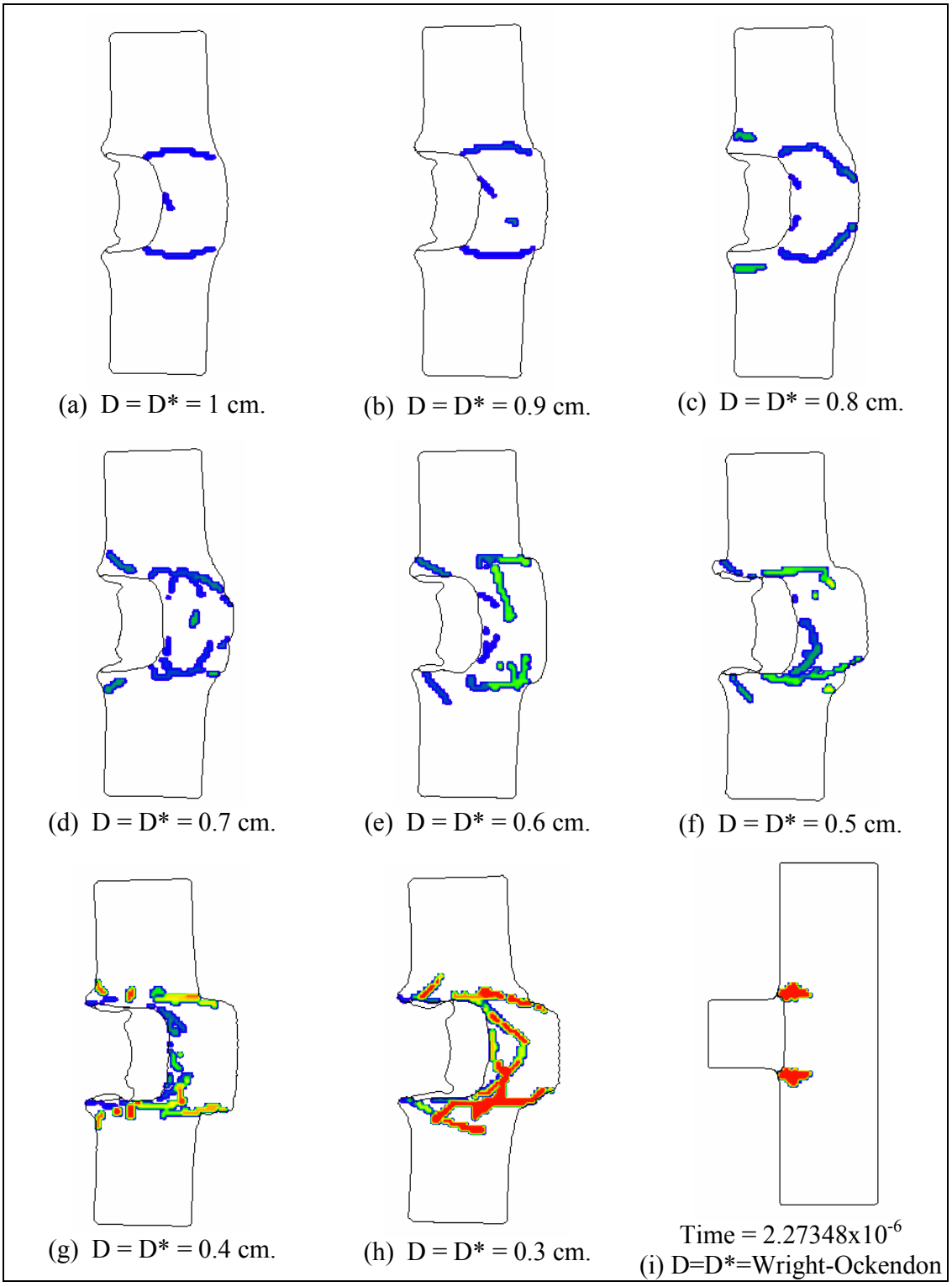

Figure 17. Effect of required minimum spacing between shear bands at time of nucleation on shear band morphology for the steel fragment impact on Ti-6Al-4V plate using the Schoenfeld-Wright criterion. No preference on nucleation locations (impact speed = 1.1 km/s). Results shown at 70 μs, except for i, as indicated.

The minimum distance requirement being varied to generate figure 17, may be viewed as an indirect control of the ease (or difficulty) of shear band nucleations in a material due to microstructure effects and resulting directional propensities, etc., that are not explicitly modeled. In that regard, proceeding from figures 17a–i provides a glimpse into the effect of gradually increasing ease of shear localizations in the material, when failure strain is kept the same. In figure 17a, plugging failure is not recognizably dominant, and the rear surface simply bulged despite that shear localizations occurred. As the distance requirement is decreased, i.e., relaxed, shear bands could nucleate more easily in the material. The overall effect is the plug shape becoming gradually more prominent, indicating an increasingly dominant plugging failure due to adiabatic shearing. A similar effect, i.e., a more pronounced protrusion on the rear surface, is observed when the Johnson-Cook fracture model is activated along with the ASB model. Note that the shear band morphology in figures 17a–c seems to be similar to the experimental results shown in figure 4a. Figure 17f is similar to the damaged sample shown in figure 4c. Since the numerical model does not exactly match the type of Ti-6Al-4V indicated in figures 4a and 4c and since the propagation speed is not physics based in the numerical model, the similarities are not regarded as validation at this time. However, a link is suggested between ease of ASB nucleation in a material, perhaps due to its microstructure, and shear band spacing. It is also indicated that shear band spacing is a critical ingredient in determining the dominant failure mode.

5. Conclusions

ASB nucleation and propagation in Ti-6Al-4V armor plates due to fragment impact at 0° obliquity were simulated in 3-D using CTH. The main objective was to assess the performance of the ASB model newly implemented into CTH and to incorporate and validate a failure model into the ASB model to make it more physics based. Progressive morphology of shear bands was captured in time, and perhaps not surprisingly, found to be sensitive to user-specified nucleation and growth criteria.

Implementation of a failure criterion by Schoenfeld and Wright effectively replaced two of the nucleation criteria, and the trial-error approach for determining the best set of critical values of nucleation strain and strain rate was eliminated. Numerical results obtained after the implementation of the criterion provided good agreement with readily available experimental evidence.

The effect of minimum spacing between shear bands on failure characteristics was studied. The capability to calculate Grady-Kipp and Wright-Ockendon length scales was incorporated into CTH to work in conjunction with the ASB model, so that they could optionally be used as a spacing requirement. For the impact geometry and conditions studied, it was observed that the minimum spacing between shear bands at the time of nucleation was loosely

bounded on the upper end with the Grady-Kipp length scale. The Grady-Kipp length scale was based on the notion that unloading caused in adjacent material of each shear band would preclude formation of other shear bands. Bounding between shear boards on the lower end was based on the Wright-Ockendon scale, where nucleating bands must be a minimum distance apart because of the influences of heat conduction and inertia. It was also observed that by relaxing the requirement for minimum spacing of shear bands at the time of nucleation, shear plugging mode of failure became more dominant.

Some of the identified areas for future work were shear band propagation velocity, direction, criteria, distance between shear bands during the growth phase, and an additional failure mechanism to work in conjunction with the shear band model to simulate crack initiation inside shear bands.

6. References

Burkins, M. S.; Love, W. W.; Wood, J. R. *Effect of Annealing Temperature on the Ballistic Limit Velocity of Ti-6Al-4V ELI*; ARL-MR-359; U.S. Army Research Laboratory: Aberdeen Proving Ground, MD, 1997.

Burkins, M. S.; Wells, M.; Fanning, J.; Roopchand, B. *The Mechanical and Ballistic Properties of an Electron Beam Single Melt of Ti-6Al-4V Plate*; ARL-MR-515; U.S. Army Research Laboratory: Aberdeen Proving Ground, MD, 2001.

Kad, B. K.; Schoenfeld, S. E.; Burkins, M. S. Through-Thickness Dynamic Impact Response in Textured Ti-6Al-4V Plates. *Materials Science and Engineering*, **2002**, *A 322*, 241–251.

Magness, L. S.; Farrand, T. G. Deformation Behavior and Its Relationship to the Penetration Performance of High-Density KE Penetrator Materials. *Proceedings of the 1990 Army Science Conference*, Durham, NC, 1990.

Nesterenko, V. F.; Meyers, M. A.; Wright, T. W. Self-Organization in the Initiation of Adiabatic Shear Bands. *Acta Materialia* **1998**, *46* (1), 327–340.

Schoenfeld, S. E.; Wright, T. W. A Failure Criterion Based On Material Instability. *International Journal of Solids and Structures* **2003**, *40*, 3021–3037.

Silling, S. A. *Shear Band Formation and Self-Shaping Penetrators*; SAND92-2692. UC-405; Sandia National Laboratories: Albuquerque, NM, February 1993.

Silling, S. A. *CTH Reference Manual: Three-Dimensional Shear Band Model* (*DRAFT*), 2002.

Weerasooriya, T.; Magness, L.; Burkins, M. Fundamental Issues of Shock-Wave and High-Strain-Rate Phenomena. *Proceedings of Explomet 2000*, Albuquerque, NM, 2001, pp 33–36.

Wright, T. W. Shear Band Susceptibility: Work Hardening Materials. *International Journal of Plasticity* **1992**, *8*, 583–602.

Wright, T. W. Toward a Defect Invariant Basis for Susceptibility to Adiabatic Shear Bands. *Mechanics of Materials* **1994**, *17*, 215–222.

Wright, T. W. *The Physics and Mathematics of Adiabatic Shear Bands*; Cambridge University Press: New York, 2002.

NO. OF COPIES	ORGANIZATION
1 (PDF Only)	DEFENSE TECHNICAL INFORMATION CTR DTIC OCA 8725 JOHN J KINGMAN RD STE 0944 FT BELVOIR VA 22060-6218
1	COMMANDING GENERAL US ARMY MATERIEL CMD AMCRDA TF 5001 EISENHOWER AVE ALEXANDRIA VA 22333-0001
1	INST FOR ADVNCD TCHNLGY THE UNIV OF TEXAS AT AUSTIN 3925 W BRAKER LN STE 400 AUSTIN TX 78759-5316
1	US MILITARY ACADEMY MATH SCI CTR EXCELLENCE MADN MATH THAYER HALL WEST POINT NY 10996-1786
1	DIRECTOR US ARMY RESEARCH LAB AMSRD ARL CS IS R 2800 POWDER MILL RD ADELPHI MD 20783-1197
3	DIRECTOR US ARMY RESEARCH LAB AMSRD ARL CI OK TL 2800 POWDER MILL RD ADELPHI MD 20783-1197
3	DIRECTOR US ARMY RESEARCH LAB AMSRD ARL CS IS T 2800 POWDER MILL RD ADELPHI MD 20783-1197

NO. OF COPIES	ORGANIZATION
	ABERDEEN PROVING GROUND
1	DIR USARL AMSRD ARL CI OK TP (BLDG 4600)

NO. OF COPIES	ORGANIZATION
4	SANDIA NATIONAL LABS DOCUMENT PROCESSING MS0617 R BELL MS0836 9116 D CRAWFORD MS0836 9116 E HERTEL MS0836 9116 S SILLING MS0820 9232 PO BOX 5800 ALBUQUERQUE NM 87185-5800
1	COMMANDER US ARMY ARMOR CENTER ATZK MW FT KNOX KY 40121-5000
2	COMMANDER US ARMY AMCOM AMSAM RD W MCCORKLE M SCHEXNAYDER REDSTONE ARSENAL AL 35898-5000
4	COMMANDER US ARMY AMCOM AMSAM RD PS WF G SNYDER (2 CPS) G JOHNSON D KIELSMEIER REDSTONE ARSENAL AL 35898-5000
1	COMMANDER US ARMY ARDEC AMSTA AR TDC J HEDDERICH PICATINNY ARSENAL NJ 07806-5000
6	COMMANDER US ARMY ARDEC AMSTA AR CCH A S MUSALLI E LOGSDON A SEBASTO M PALATHINGAL S GHAZI R CARR PICATINNY ARSENAL NJ 07806-5000
1	COMMANDER US ARMY ARDEC AMSTA AR FSP I R COLLETT PICATINNY ARSENAL NJ 07806-5000
3	PROJECT MANAGER MANEUVER AMMUNITION SYS AMO MAS R DARCY D GUZIEWICZ W SANVILLE PICATINNY ARSENAL NJ 07806-5000
3	COMMANDER US ARMY NGIC LANG SCC W GSTATTENBAUER J MORGAN R AIKEN 220 SEVENTH ST NE CHARLOTTESVILLE VA 22902-5396
2	COMMANDER US ARMY RESEARCH OFFICE J BAILEY S F DAVIS PO BOX 12211 RESEARCH TRIANGLE PARK NC 27709-2211
12	COMMANDER NAVAL SURFACE WARFARE CTR DAHLGREN DIV H CHEN D L DICKINSON CODE G24 C R ELLINGTON C R GARRETT CODE G22 W HOLT CODE G22 W HOYE G22 R MCKEOWN J NELSON M J SILL CODE H11 W J SROTHER A WARDLAW JR L WILLIAMS CODE G33 17320 DAHLGREN RD DAHLGREN VA 22448
2	AIR FORCE ARMAMENT LAB AFATL DLJR J FOSTER D LAMBERT EGLIN AFB FL 32542-6810

NO. OF
COPIES ORGANIZATION

1 USAF PHILLIPS LAB
VTSI
R ROYBAL
KIRTLAND AFB NM 87117-7345

ABERDEEN PROVING GROUND

1 DIR USAAMSAA
T THOMPSON
BLDG 392
APG MD 21005

33 DIR USARL
AMSRD SL BE
L ROACH
AMSRD WM
T ROSENBERGER
J SMITH
T WRIGHT
AMSRD WM BP
E SCHMIDT
AMSRD WM T
B BURNS
AMSRD WM TA
M BURKINS
R DONEY
T HAVEL
D KLEPONIS
M NORMANDIA
J RUNYEON
M ZOLTOSKI
AMSRD WM TB
P BAKER
J STARKENBERG
AMSRD WM TC
R COATES
M FERMEN-COKER (4 CPS)
K KIMSEY
L MAGNESS
D SCHEFFLER
S SCHRAML
B SORENSEN
AMSRD WM TD
T W BJERKE
D CASEM
H W MEYER
M RAFTENBERG
S SCHOENFELD
S SEGLETES
T WEERASOORIYA
AMSRD WM TE
J POWELL

INTENTIONALLY LEFT BLANK.